

August 27, 2014

# **Development of an aerosol microphysical module: Aerosol Two-dimensional bin module for foRmation and Aging Simulation (ATRAS)**

H. Matsui,<sup>1</sup> M. Koike,<sup>2</sup> Y. Kondo,<sup>2</sup> J. D. Fast,<sup>3</sup> and M. Takigawa<sup>1</sup>

<sup>1</sup> Japan Agency for Marine-Earth Science and Technology, Kanagawa, Japan

<sup>2</sup> Department of Earth and Planetary Science, Graduate School of Science, University of Tokyo, Tokyo, Japan

<sup>3</sup> Pacific Northwest National Laboratory, Richland, Washington, USA

14 Short title: MATSUI ET AL.: 2D AEROSOL BIN MODULE, ATRAS

Correspondence to: H. Matsui ([matsui@jamstec.go.jp](mailto:matsui@jamstec.go.jp))

Submitted to Atmospheric Chemistry and Physics: 12 March, 2014

**Revised following reviewers' comments: 27 August, 2014**

20    **Abstract**

21    Number concentrations, size distributions, and mixing states of aerosols are essential  
22    parameters for accurate estimations of aerosol direct and indirect effects. In this study,  
23    we develop an aerosol module, designated the Aerosol Two-dimensional bin module for  
24    foRmation and Aging Simulation (ATRAS), that can explicitly represent these parameters  
25    by considering new particle formation (NPF), black carbon (BC) aging, and secondary  
26    organic aerosol (SOA) processes. A two-dimensional bin representation is used for  
27    particles with dry diameters from 40 nm to 10  $\mu\text{m}$  to resolve both aerosol sizes (12 bins)  
28    and BC mixing states (10 bins) for a total of 120 bins. The particles with diameters  
29    between 1 and 40 nm are resolved using additional 8 size bins to calculate NPF. The  
30    ATRAS module is implemented in the WRF-chem model and applied to examine the  
31    sensitivity of simulated mass, number, size distributions, and optical and radiative  
32    parameters of aerosols to NPF, BC aging and SOA processes over East Asia during the  
33    spring of 2009. The BC absorption enhancement by coating materials is about 50% over  
34    East Asia during the spring, and the contribution of SOA processes to the absorption  
35    enhancement is estimated to be 10 – 20% over northern East Asia and 20 – 35% over  
36    southern East Asia. A clear north-south contrast is also found between the impacts of  
37    NPF and SOA processes on cloud condensation nuclei (CCN) concentrations: NPF  
38    increases CCN concentrations at higher supersaturations (smaller particles) over northern  
39    East Asia, whereas SOA increases CCN concentrations at lower supersaturations (larger  
40    particles) over southern East Asia. The application of ATRAS in East Asia also shows  
41    that the impact of each process on each optical and radiative parameter depends strongly  
42    on the process and the parameter in question. The module can be used in the future as

43 a benchmark model to evaluate the accuracy of simpler aerosol models and examine  
44 interactions between NPF, BC aging, and SOA processes under different meteorological  
45 conditions and emissions.

46

47     **1. Introduction**

48         Atmospheric aerosols play an important role in Earth's climate system by  
49         scattering and absorbing solar radiation (direct effects) and by modifying the  
50         microphysical properties of clouds and precipitation (indirect effects). Estimates of  
51         these direct and indirect effects remain highly uncertain, and they are one of the largest  
52         uncertainties in predicting climate change (Ramanathan et al., 2001; Lohmann and  
53         Feichter, 2005; Bond et al., 2013; IPCC, 2013).

54         Accurate estimations of these effects by a model require good representations of  
55         aerosol number concentrations, size distributions, and mixing states because these  
56         parameters are essential for calculating aerosol absorption and scattering coefficients and  
57         for calculating the number concentrations of cloud droplets activated from aerosols  
58         (Jacobson, 2000; Ghan et al., 2011; Reddington et al., 2011). However, many of the  
59         existing three-dimensional aerosol models do not represent these aerosol parameters  
60         sufficiently. These models predict mass concentrations but diagnose size distributions,  
61         number concentrations, or both by assuming variable or predetermined lognormal size  
62         distributions. A model that can predict aerosol number concentrations, size distributions,  
63         and mixing states should be useful for reducing the uncertainties in the estimates of  
64         aerosol contributions to climate change.

65         Various physical and chemical processes play important roles in controlling the  
66         number concentrations, size distributions, and mixing states of aerosols in the atmosphere.  
67         New particle formation (NPF), which is the formation of ultrafine particles ( $\sim 1$  nm in  
68         diameter) and their subsequent growth, is considered to have a large impact on aerosol  
69         number concentrations and cloud condensation nuclei (CCN) concentrations and

70 ultimately on cloud droplet number concentrations and the indirect effects of aerosols  
71 (Kulmala et al., 2000, 2004, 2007; Spracklen et al., 2006, 2008, 2010; Merikanto et al.,  
72 2009, Makkonen et al., 2009, 2012). Aging processes (i.e., condensation, coagulation,  
73 and photochemical oxidation) of black carbon (BC) particles enhance their absorption  
74 efficiency and CCN activity, and they increase the heating rate of the atmosphere and the  
75 wet scavenging efficiency of BC and modify the microphysical properties of clouds  
76 (Jacobson, 2000, 2001; Bond et al., 2006, 2013; Stier et al., 2006; Moteki et al., 2007).  
77 Resolving externally-mixed BC, internally-mixed BC, and BC-free particles is essential  
78 for accurately estimating BC radiative and cloud microphysical effects (Oshima et al.,  
79 2009; Aquila et al., 2011; Matsui et al., 2013a). Organic aerosol (OA) formation, which  
80 has been severely underestimated in many existing three-dimensional aerosol models  
81 (Heald et al., 2005, 2011; Matsui et al., 2009a; Spracklen et al., 2011), is also important  
82 in terms of the mass concentration and CCN activity of aerosols (Kanakidou et al., 2005;  
83 Zhang et al., 2007; Hallquist et al., 2009).

84 In our previous studies, we developed modules for NPF, BC aging, and  
85 secondary OA (SOA) processes individually using the Weather Research and Forecasting  
86 and Chemistry (WRF-chem) model (Matsui et al., 2011, 2013a, 2013b, 2014). These  
87 modules succeeded in explaining important aerosol properties related to number  
88 concentrations, size distributions, and mixing states of aerosols in the atmosphere. Our  
89 NPF-resolved aerosol module (Matsui et al., 2011) can calculate condensational growth  
90 and coagulation sink of nucleated particles with 20 aerosol size bins from 1 nm to 10  $\mu\text{m}$   
91 in diameter, and the module reproduced the timing of NPF events in the Beijing region of  
92 China. Our BC mixing state resolved aerosol module (Matsui et al., 2013a) calculates

93 BC aging processes using a two-dimensional aerosol bin representation ( $12 \times 10$  bins)  
94 that resolves both aerosol sizes (from 40 nm to  $10 \mu\text{m}$  in diameter) and BC mixing states  
95 (pure-BC particles, BC-free particles, and 8 different internally-mixed BC particles).  
96 This module reproduced the features of the BC mixing state observed by a single-particle  
97 soot photometer (SP2) during the Aerosol Radiative Forcing in East Asia (A-FORCE)  
98 aircraft campaign, and it was used to evaluate the impact of the treatment of BC mixing  
99 state on radiative and microphysical properties of BC over the East Asian region. Our  
100 SOA scheme (Matsui et al., 2014), which is based on the volatility basis-set approach  
101 (Donahue et al., 2006; Jimenez et al., 2009), reproduced mass concentrations and  
102 temporal variations of OA over East Asia reasonably well.

103 Our previous studies showed the improvement of model performance for NPF,  
104 BC aging, and SOA processes by using a detailed aerosol model. A detailed model is  
105 useful, particularly when detailed aerosol parameters are compared between  
106 measurements and model simulations because it is conceptually better (e.g., Korhola et  
107 al., 2014) and uses less assumption than a simple model. With the development of more  
108 advanced observational techniques, we need more detailed and sophisticated  
109 representations in aerosol models for comparisons.

110 In this study, we develop an aerosol module that can calculate NPF, BC aging,  
111 and SOA processes simultaneously. The module, designated the Aerosol Two-  
112 dimensional bin module for foRmation and Aging Simulation (ATRAS), is implemented  
113 in the WRF-chem model. Few three-dimensional aerosol models can calculate NPF, BC  
114 aging, and SOA processes simultaneously (Yu et al., 2012). To our knowledge, ATRAS  
115 can calculate these processes simultaneously with the most detailed treatment of BC aging

116 processes. Here, we describe the ATRAS module (Sect. 2) and present the first results  
117 of its application over East Asia to examine the sensitivity of mass, number, size  
118 distributions, and optical and radiative parameters of aerosols to NPF, BC aging, and SOA  
119 processes (Sect. 3).

120

## 121 **2. The two-dimensional bin module: ATRAS**

122 The ATRAS module is developed using the framework of the WRF-chem model  
123 (version 3.4) (Grell et al., 2005; Skamarock et al., 2008), and it is used in combination  
124 with the Model for Simulating Aerosol Interactions and Chemistry (MOSAIC) aerosol  
125 module (Fast et al., 2006; Zaveri et al., 2008) (hereafter referred to as WRF-  
126 chem/ATRAS-MOSAIC). We used the WRF-chem/MOSAIC model in our previous  
127 studies (Matsui et al., 2009b, 2010, 2011, 2013a, 2013b, 2014).

128 The ATRAS module uses 128 aerosol bins in total (Fig. 1). A two-dimensional  
129 bin representation is used for particles with dry diameters from 40 nm to 10  $\mu\text{m}$  to resolve  
130 both aerosol sizes and BC mixing states. As in our BC mixing state-resolved aerosol  
131 module (Matsui et al., 2013a), the aerosol sizes from 40 nm to 10  $\mu\text{m}$  are divided into 12  
132 bins, and the BC mixing state is divided into 10 bins using the fraction of the BC mass to  
133 the total aerosol mass concentrations under dry conditions. Within this size range, the  
134 module can resolve pure-BC particles (BC mass fraction > 0.99), BC-free particles (BC  
135 mass fraction = 0), and 8 different internally-mixed BC particles (BC mass fractions of 0  
136 – 0.1, 0.1 – 0.2, 0.2 – 0.35, 0.35 – 0.5, 0.5 – 0.65, 0.65 – 0.8, 0.8 – 0.9, and 0.9 – 0.99).  
137 The particles from 1 to 40 nm are resolved using 8 size bins to calculate NPF. Particles  
138 in this size range are assumed to be BC free. The module therefore uses 128 bins (12  $\times$

139 10 + 8 bins) to represent aerosol sizes, BC mixing states, and NPF processes. Mass  
140 concentrations of sulfate, nitrate, ammonium, BC, OA (sum of primary and secondary),  
141 dust, sodium, chloride, and aerosol water and number concentrations are traced in each  
142 aerosol bin. Aerosols in the aerosol-phase (interstitial) and the cloud-phase are treated  
143 separately using additional 128 bins for cloud-phase (activated) aerosols (in total 256 bins  
144 are used to represent aerosols).

145 Primary aerosol emissions (BC and OA in this study) are treated as pure-BC or  
146 BC-free particles from 40 nm to 10  $\mu\text{m}$ . The uncertainty of mixing state treatment in  
147 emissions is described by Matsui et al. (2013a). Gas-phase chemistry is calculated by  
148 the SAPRC-99 mechanism (Carter, 2000) with modification for SOA precursors (Matsui  
149 et al., 2014). The particle formation (nucleation) rate at 1 nm is estimated by activation-  
150 type (e.g., Kulmala et al., 2006) or kinetic nucleation (e.g., Kuang et al., 2008) in the  
151 boundary layer and by a binary ( $\text{H}_2\text{SO}_4$ -water) homogeneous nucleation (Wexler et al.,  
152 1994) in the free troposphere, as described by Matsui et al. (2011). In this study, we use  
153 the activation-type nucleation (nucleation rate at 1 nm is proportional to  $\text{H}_2\text{SO}_4$   
154 concentrations) with a constant rate coefficient of  $2 \times 10^{-7} \text{ s}^{-1}$ , which was adopted in our  
155 previous studies (Matsui et al., 2011, 2013c). Condensation and evaporation are  
156 calculated by the MOSAIC module (Zaveri et al., 2005a, 2005b, 2008). Aqueous-phase  
157 chemistry is calculated by the scheme developed by Fahey and Pandis (2001). The shift  
158 of bins due to condensation, evaporation, and aqueous-phase chemistry is calculated by a  
159 two-moment (mass and number) advection scheme (Simmel and Wurzler, 2006) for  
160 aerosol size bins and the moving center approach (Jacobson, 1997) for mixing state bins,  
161 as described by Matsui et al. (2013a). Brownian coagulation within two-dimensional

162 bins is calculated using the method of Matsui et al. (2013a), which is based on the semi-  
163 implicit method of Jacobson et al. (1994).

164 SOA processes are calculated by the volatility basis-set scheme with  
165 photochemical multigenerational oxidation of organic vapors by OH radicals (Matsui et  
166 al., 2014), which is similar in many respects to Shrivastava et al. (2011). This scheme  
167 uses 9 volatility classes to represent semi-volatile and intermediate volatility organic  
168 compounds (S/IVOCs). We consider the formation of first-generation oxidized VOCs  
169 (OVOCs) from 9 lumped VOCs; alkanes (ALK4 and ALK5), olefins (OLE1 and OLE2),  
170 aromatics (ARO1 and ARO2), isoprene (ISOP), monoterpene (TERP), and sesquiterpene  
171 (SESQ). The mass yield of OVOCs from each lumped VOC is calculated with a NO<sub>x</sub>-  
172 dependent 4-product basis fit (Tsimpidi et al., 2010). S/IVOCs and OVOCs are oxidized  
173 to the volatility class with an order of magnitude lower effective saturation concentrations  
174 by OH radicals at a rate constant of  $1 \times 10^{-11} \text{ cm}^3 \text{ molecule}^{-1} \text{ s}^{-1}$ . Size-resolved OA  
175 condensation and evaporation are calculated using the method of Koo et al. (2003) by  
176 assuming gas-particle equilibrium partitioning (Schell et al., 2001). Dry deposition and  
177 wet deposition of both gaseous and aerosol species are calculated using the method  
178 adopted in the original WRF-chem/MOSAIC model (Easter et al., 2004). Aerosol  
179 activation to cloud droplets is calculated on the basis of the method described by Abdul-  
180 Razzak and Ghan (2000) through the calculation of volume-averaged hygroscopicity and  
181 critical supersaturation for each aerosol bin (Matsui et al., 2011, 2013a). The values of  
182 hygroscopicity ( $\kappa$ ) for each aerosol species are given by Matsui et al. (2011). A  $\kappa$  value  
183 of 0.14 is assumed for all the OA species used in the volatility basis-set scheme (Matsui  
184 et al., 2014). In Table 1, the schemes and the representation used in ATRAS-MOSAIC

185 are summarized and compared with those of the original WRF-chem/MOSAIC model.  
186 More details of the WRF-chem/MOSAIC model and the MOSAIC module are described  
187 by Fast et al. (2006) and Zaveri et al. (2008), respectively. More details of the NPF, BC  
188 aging, and SOA schemes are described by Matsui et al. (2011, 2013a, 2013b, 2014).

189

190 **3. Application of ATRAS-MOSAIC to East Asia**

191 **3.1. Simulation settings**

192 Our previous WRF-chem simulations were conducted over East Asia during the  
193 A-FORCE aircraft campaign (21 March – 26 April 2009) (Matsui et al., 2013a, 2013b,  
194 2014). In these studies, aerosol mass and number concentrations and their spatial and  
195 temporal variations were evaluated using both aircraft and surface measurements. In  
196 this study, the ATRAS-MOSAIC model is applied to this region and period. Statistics  
197 are calculated for the period from 24 March to 26 April 2009 (34 days).

198 The simulation domain consists of an outer domain with a horizontal grid  
199 spacing of 360 km and an inner domain with a horizontal grid spacing of 120 km; there  
200 are 13 vertical layers up to 100 hPa (Fig. 2a). Because the ATRAS-MOSAIC module is  
201 computationally expensive, a relatively coarse grid resolution is used. However, our  
202 previous simulations using the same resolution reasonably well reproduced  
203 meteorological fields associated with synoptic-scale meteorological variations and  
204 resulting aerosol transport and variation processes during the A-FORCE period (Matsui  
205 et al., 2013a). The results for the inner domain are described in this paper. We use the  
206 National Centers for Environmental Prediction Final Operational Global Analysis data  
207 for initial and boundary conditions and for nudging (free troposphere only) of

208 meteorological fields. The meteorological schemes adopted in this study are similar to  
209 those used by Matsui et al. (2009, 2014).

210 In this study, aerosol optical and radiative parameters (shown in section 3.4) are  
211 calculated offline using the method of Matsui et al. (2013a). Local aerosol optical  
212 properties are calculated using the Mie theory algorithm developed by Bohren and  
213 Huffman (1998). The shell-core treatment (BHOAT) is used for internally mixed BC  
214 particles, while the code for well-mixed particles (BHMIE) is applied to pure BC and BC-  
215 free particles (Matsui et al., 2013a). The enhancement of BC absorption (the lens effect)  
216 by coating material (other than BC) is calculated in the BHOAT. Radiative feedback  
217 of aerosols to meteorological parameters (e.g., temperature) is not considered in this study.  
218 Aerosol indirect effect is considered to calculate aerosol activation and removal processes  
219 theoretically. This treatment influences cloud microphysics and distribution, but we do  
220 not focus on these changes in this study. Radiative calculations are performed for clear-  
221 sky conditions (section 3.4).

222 Emission inventories are also similar to those of Matsui et al. (2014): the  
223 anthropogenic and volcanic emissions of Streets et al. (2003), biomass burning emissions  
224 of the Global Fire Emissions Database version 3 (GFED3) (van der Werf et al., 2010),  
225 and the online biogenic emissions of the Model of Emissions of Gases and Aerosols from  
226 Nature version 2 (MEGAN2) (Guenther et al., 2006). A number median diameter of 50  
227 nm and a standard deviation ( $\sigma$ ) of 2.0 are assumed as the size distribution of primary  
228 aerosol emissions (Matsui et al., 2013a). Emissions of coarse particles are not  
229 considered in this study.

230 We conduct nine model simulations (Table 2). The M10\_SN simulation, which

231 is the most detailed simulation with BC aging (M) with 10 BC mass fractions, SOA (S),  
232 and NPF (N), is used as the benchmark simulation in this study. The M08\_SN, M06\_SN,  
233 M04\_SN, and M01\_SN simulations are runs with different numbers of BC mixing state  
234 bins and include NPF and SOA. BC mixing state bins are divided into BC mass  
235 fractions of 0, 0 – 0.1, 0.1 – 0.2, 0.2 – 0.5, 0.5 – 0.8, 0.8 – 0.9, 0.9 – 0.99, and 0.99 – 1.0  
236 in the M08\_SN simulation; 0, 0 – 0.2, 0.2 – 0.5, 0.5 – 0.8, 0.8 – 0.99, and 0.99 – 1.0 in  
237 the M06\_SN simulation; and 0, 0 – 0.8, 0.8 – 0.99, 0.99 – 1.0 in the M04\_SN simulation.  
238 These simulations are compared with the M10\_SN simulation to examine the sensitivity  
239 of the mass and number concentrations and optical and radiative parameters of aerosols  
240 to the number of BC mixing state bins. The M10\_N simulation (OA is from primary  
241 emissions only) is compared with the M10\_SN simulation to examine the impact of SOA  
242 processes on BC mixing states. The M01\_N, M01\_S, and M01 simulations are  
243 conducted to determine the impact of NPF and SOA processes on aerosol properties.  
244 The M10\_SN and M01 simulations are compared to understand the overall effects of NPF,  
245 BC aging, and SOA processes on aerosol properties. The M01\_S simulation is nearly  
246 the same as the base simulation described by Matsui et al. (2014), except for the number  
247 of aerosol size bins (8 size bins for the simulation described in Matsui et al. (2014) versus  
248 12 size bins in M01\_S). The CPU time required for the M10\_SN simulation is about 36  
249 hours per simulation day in our application (SGI ICE X (Intel Xeon E5-2670 2.6GHz,  
250 SUSE Linux Enterprise Server 11SP1, Intel Composer XE 12)). Compared with the  
251 original 8-bin MOSAIC simulation, the computational costs are 14, 3.5, and 1.7 times  
252 greater in the M10\_SN, M01\_SN, and M01 simulations, respectively.

253

254        **3.2. Comparison with measurements**

255            We showed detailed validation results for various aerosol parameters obtained  
256        by surface and aircraft measurements (Fig. 2b) in our previous studies (Matsui et al.,  
257        2013a, 2013b, 2014). Although the simulation setups in this study are not exactly the  
258        same as those in our previous studies (e.g., grid spacing, gas-phase chemistry mechanism,  
259        and amounts and size distributions of emissions), similar or better model performances  
260        are obtained for the following aerosol parameters in the benchmark M10\_SN simulation  
261        (Fig. 3 and Fig. S1-S3): BC, sulfate, and OA mass concentrations at Fukue (32.75°N,  
262        128.68°E) and Hedo (26.87°N, 128.25°E) in Japan (outflow region from the Asian  
263        continent) (Matsui et al., 2013a, 2014); mass and number concentrations of BC and  
264        scattering aerosols (other than BC) and their vertical profiles, BC mixing states (the shell-  
265        to-core diameter ratio at a BC core diameter of 200 nm), and aerosol number  
266        concentrations (> 10 nm) in the boundary layer during the A-FORCE campaign (Matsui  
267        et al., 2013a, 2013b). We note that the model performance improved for the shell-to-  
268        core diameter ratio during the A-FORCE campaign by considering SOA processes (Fig.  
269        3). Details of the measurements during A-FORCE are given elsewhere (Moteki and  
270        Kondo, 2007, 2010; Kondo et al., 2011; Oshima et al., 2012; Moteki et al., 2012;  
271        Takegawa et al., 2013; Takami et al., 2005, 2007; Kanaya et al., 2013).

272

273        **3.3. Aerosol mass and number concentrations and size distributions**

274            The spatial distributions of period-averaged concentrations of PM<sub>2.5</sub> (particulate  
275        matter smaller than 2.5 μm in diameter) in the M10\_SN and M01 simulations at an  
276        altitude of about 1 km (sigma level of 0.895) are shown in Fig. 4a,b, and statistics are

277 shown in Table 3. Period-averaged values are calculated using the data at 12:00 local  
278 time (03:00 UTC) during the simulation periods (24 March – 26 April). The conclusions  
279 obtained in this section do not change even when using the data at night (00:00 local time)  
280 (not shown). The period- and domain-averaged PM<sub>2.5</sub> concentrations are 15.1 and 12.1  
281  $\mu\text{g m}^{-3}$  in the M10\_SN and M01 simulations, respectively. The higher PM<sub>2.5</sub>  
282 concentrations in the M10\_SN simulation (about 25% higher) are mostly due to SOA  
283 processes considering that the PM<sub>2.5</sub> concentrations are different between the simulations  
284 with and without SOA processes (Table 3). The treatment of BC mixing state and NPF  
285 has a negligible impact on the period-averaged PM<sub>2.5</sub> in our simulations. As emissions  
286 of coarse particles are not considered in this study (Sect. 3.1), most of PM<sub>2.5</sub> is PM<sub>1</sub> in  
287 our simulation: the period- and domain-averaged PM<sub>1</sub> concentrations are 14.7  $\mu\text{g m}^{-3}$  in  
288 the M10\_SN simulation.

289 BC mass concentrations are influenced by the treatment of the BC mixing state  
290 (Table 3). BC mass concentration in the M10\_SN simulation is higher than that in the  
291 M01\_SN simulation because pure BC is explicitly resolved in the M10\_SN simulation,  
292 whereas all BC is treated as internally-mixed particles in the M01\_SN simulation,  
293 resulting in a higher wet removal efficiency (Matsui et al., 2013a). BC concentrations  
294 in the M08\_SN and M06\_SN simulations are nearly the same as those in the benchmark  
295 M10\_SN simulation. These two simulations can explain more than 90% of the total  
296 effect of BC mixing state (Table 3). The percentage is calculated from the difference in  
297 the BC mass concentrations between the M08\_SN (or M06\_SN) and M01\_SN  
298 simulations relative to the difference between the M10\_SN and M01\_SN simulations.  
299 BC concentration in the M04\_SN simulation is also generally consistent with that in the

300 benchmark simulation: the M04\_simulation can explain about 70% of the total effect of  
301 the BC mixing state. These results suggest that the simulations with 4 or more mixing  
302 state bins can explain the actual BC mixing state effect reasonably well in terms of the  
303 BC mass concentrations in the boundary layer. The treatments of NPF and SOA have a  
304 negligible impact on the period-averaged BC mass concentrations in our simulations.

305 OA mass concentrations differ substantially (by a factor of 3) between the  
306 simulations with and without SOA processes. The period- and domain-averaged OA  
307 concentrations are about 4.3 and 1.5  $\mu\text{g m}^{-3}$  in the simulations with and without SOA  
308 processes, respectively (Table 3).

309 The CCN concentrations for two given supersaturations of 1.0% (CCN<sub>1.0</sub>) and  
310 0.1% (CCN<sub>0.1</sub>) are calculated based on Köhler theory (Matsui et al., 2011). The spatial  
311 distributions of the period-averaged CCN<sub>1.0</sub> for the M10\_SN and M01 simulations at an  
312 altitude of about 1 km are shown in Fig. 4c,d. The CCN<sub>1.0</sub> distributions in the M10\_SN  
313 (M01) simulations are generally similar to those in the simulations with (without) NPF in  
314 Matsui et al. (2013b), although some model setups differ between Matsui et al. (2013b)  
315 and this study (e.g., grid resolution and gas-chemistry mechanism). Period- and  
316 domain-averaged CCN<sub>1.0</sub> concentrations increase by 18% when both NPF and SOA  
317 processes are included (Table 3). The spatial distributions of the period-averaged  
318 CCN<sub>0.1</sub> are shown in Fig. 4e,f. The period- and domain-averaged CCN<sub>0.1</sub> concentrations  
319 increase by 16% when both NPF and SOA processes are included (Table 3). The  
320 treatment of BC mixing state is not particularly important for either CCN<sub>1.0</sub> or CCN<sub>0.1</sub>  
321 concentrations.

322 dCCN is defined as the difference in the CCN concentrations between M01\_N

323 and M01 (an index of the importance of NPF) or between M01\_S and M01 (an index of  
324 the importance of SOA). There is a clear contrast in the importance between NPF and  
325 SOA processes. NPF increases CCN<sub>1.0</sub> concentrations considerably, whereas SOA  
326 makes only a minor contribution to the increase in CCN<sub>1.0</sub> concentrations (Fig. 5a,b).  
327 The increase in CCN<sub>1.0</sub> concentrations due to NPF is distributed mainly over the northern  
328 part of the simulation domain (northern and central China, Korea, and Japan; Fig. 5a).  
329 This result is consistent with the results reported by Matsui et al. (2013b), who showed a  
330 clear north-south contrast in the NPF frequency over East Asia (Fig. S4). In contrast,  
331 SOA is much more important for CCN<sub>0.1</sub> concentrations, whereas the impact of NPF on  
332 CCN<sub>0.1</sub> concentrations is limited (Fig. 5c,d). The increase in CCN<sub>0.1</sub> concentrations due  
333 to SOA is mainly seen over the southern part of the simulation domain (Southeast Asia  
334 and southern China; Fig. 5d), where SOA concentrations and their ratio to preexisting  
335 aerosols are high (e.g., SOA/BC ratio in Fig. S4). These results show that NPF is an  
336 important factor for increasing CCN concentrations at higher supersaturations (smaller  
337 particles) over northern East Asia, whereas SOA is an important factor for increasing  
338 CCN concentrations at lower supersaturations (larger particles) over southern East Asia.  
339 This difference might also imply that NPF and SOA processes have spatially different  
340 influences on cloud microphysical properties over East Asia, although we do not focus  
341 on the indirect effects of aerosols in this study.

342 An increase in BC mass concentrations at an altitude of about 1 km is seen for  
343 particles of around 100 – 500 nm in the accumulation mode when the BC mixing state is  
344 resolved (M10\_SN and M04\_SN in Fig. 6a). SOA processes increase OA mass  
345 concentrations of around 100 – 500 nm with a shift to a larger size distribution (Fig. 6b).

346 Total (bulk) mass concentrations of inorganic species are not particularly influenced by  
347 NPF, BC aging, or SOA processes (Table 3), but the size distributions of these species are  
348 shifted to larger sizes, mainly due to SOA processes (Fig. 6c). Number size distribution  
349 is influenced by both NPF and SOA processes (Fig. 6d). NPF has a large impact on the  
350 number concentrations of particles less than 100 nm in diameter (e.g., comparing the  
351 M01\_N and M01 simulations), although condensation is the dominant process in terms  
352 of mass transfer from gas to the aerosol phase (the mass fraction of sulfate between 1 and  
353 40 nm is only 0.07% of total sulfate mass on period and domain average at 1 km). OA  
354 formation shifts the size distribution to larger sizes (e.g., comparing the M01\_S and M01  
355 simulations), with the increase in the number concentrations of particles of around 200 –  
356 400 nm and the decrease in the number concentrations of particles of around 30 – 100 nm.  
357 The combined effects of NPF and SOA are reflected in the benchmark simulation  
358 (M10\_SN).

359 Sensitivity simulations with 4 and 6 NPF bins between 1 and 40 nm show that  
360 they can capture the growth of nucleated particles and absolute number concentrations  
361 and their size distributions less than 40 nm in diameter reasonably well (Fig. S5). These  
362 results suggest that 4 NPF bins between 1 and 40 nm may be sufficient for future  
363 applications.

364 We focused on the period-averaged contributions of individual processes in this  
365 section, but their impacts could be much larger locally and temporarily. For example,  
366 while BC concentration in the M10\_SN simulation is about 20% higher than that in the  
367 M01\_SN simulation on period- and domain-average, the concentration is more than 40%  
368 higher at particular places and times (Fig. S6). Even though the impact of a process is

369 small on period- and domain-average (the concentration ratio is about 1.0 in Fig. S6), the  
370 process can contribute to an increase or decrease in mass and/or number concentrations  
371 at particular places and times (Fig. S6).

372 The vertical profiles of CCN and mass concentrations show that the features  
373 obtained at an altitude of about 1 km (layer 4) are seen at all levels (Fig. 7): OA and  
374 CCN<sub>0.1</sub> concentrations are higher in the simulations with the OA formation scheme, BC  
375 mass concentrations are higher in the simulations that resolve mixing states, and CCN<sub>1.0</sub>  
376 concentrations are higher in the simulations with NPF.

377

### 378 **3.4. Aerosol optical and radiative parameters**

379 Period-averaged optical and radiative parameters are calculated using the data at  
380 12:00 local time during the simulation period (24 March – 26 April). We focus on  
381 column aerosol optical depth (AOD), column absorption AOD (AAOD), single scattering  
382 albedo (SSA) at 1 km, heating rate by aerosols at 1 km, and change in downward solar  
383 flux by aerosols at the surface. The statistics are shown in Table 4.

384 Period- and domain-averaged AOD is increased by 26% by SOA processes  
385 (Table 4). The impact of NPF and BC aging processes on AOD is negligible in our  
386 simulations.

387 The treatment of BC mixing state is important for AAOD, SSA, and heating rate.  
388 The column AAOD, the fraction of absorption ( $1 - \text{SSA}$ ) at 1 km, and the heating rate at  
389 1 km are 16%, 50%, and 17% higher, respectively, in the M01 simulation (domain  
390 average) than in the benchmark M10\_SN simulation. The difference in absorption  
391 between the two simulations is attributed to two effects: the M01 simulation has (1) higher

392 absorption by coating materials (lens effect) and (2) lower BC mass concentrations due  
393 to efficient wet removal processes (which decreased absorption) than the M10\_SN  
394 simulation because the M01 simulation assumes internally mixing for all BC particles.  
395 These effects on absorption partly cancel each other because of their opposite signs (Stier  
396 et al., 2006; Matsui et al., 2013a). Because the former effect is larger than the latter  
397 effect in this study, the absorption in the M01 simulation is larger than that in the  
398 benchmark simulation.

399 Column AAOD is high over both northern and southern China (Fig. 8a). We  
400 calculated the absorption enhancement ratio by the lens effect for the M10\_SN and  
401 M10\_N simulations (Fig. 8b). In calculating the AAOD values with the assumption of  
402 externally-mixed BC particles, all of the internally-mixed BC particles are separated into  
403 BC (externally-mixed) and non-BC (BC-free) particles. The absorption enhancement  
404 ratio is estimated to be about 50 – 60% and 40% in the M10\_SN and M10\_N simulations,  
405 respectively (Fig. 8b). Because the absorption enhancement ratio is about 100% in the  
406 M01\_SN simulation (not shown), the simulation without BC mixing states (internally-  
407 mixed treatment for all particles) overestimates the absorption enhancement by a factor  
408 of 2. The contribution of SOA processes (the difference in AAOD between M10\_SN  
409 and M10\_N) to the total absorption enhancement is about 20% over northern East Asia  
410 and about 20 – 40% over southern East Asia (Fig. 8c). A reason of this latitudinal  
411 dependency is higher OA/BC mass ratio over southern East Asia (Fig. S4).

412 The difference in SSA between the benchmark and M01 simulations is caused  
413 by both BC aging and SOA processes. The treatment of BC mixing state increases SSA  
414 by 0.05 over northern China (30 – 45°N) (Fig. 9a), where BC concentrations are high (Fig.

415 S4). The treatment of SOA processes is estimated to increase SSA by 0.03 at latitudes  
416 of  $30 - 40^{\circ}\text{N}$ , where both BC and OA concentrations are high, mainly due to the  
417 enhancement of the scattering coefficient (Fig. 9b).

418 The difference in the heating rate by aerosols between the benchmark and M01  
419 simulations is caused by two opposite effects. The treatment of the BC mixing state  
420 decreases the heating rate by  $0.3 \text{ K d}^{-1}$ , mainly over northern China ( $30 - 40^{\circ}\text{N}$ ) due to  
421 the reduction of absorption (Fig. 9c). SOA processes increase the heating rate by  $0.1 \text{ K}$   
422  $\text{d}^{-1}$  over central and southern China ( $20 - 35^{\circ}\text{N}$ , Fig. 9d), where OA concentrations are  
423 high, because SOA processes increase the multiple scattering of radiation and the lens  
424 effect (Fig. 8c), both of which can enhance absorption.

425 The difference in the downward solar flux at the surface between the benchmark  
426 and M01 simulations is also caused by two opposite effects. SOA processes decrease  
427 the downward flux at the surface by  $15 \text{ W m}^{-2}$ , with a maximum decrease over southern  
428 China ( $20 - 30^{\circ}\text{N}$ , Fig. 9f) where OA concentrations are high. The treatment of BC  
429 mixing state increases the flux by  $5 \text{ W m}^{-2}$ , with a maximum increase over central China  
430 (Fig. 9e). The increase is attributed to reduced absorption in the benchmark simulation  
431 that leads to increased multiple scattering of radiation and downward surface flux.

432 The spatial distributions of the combined effects of BC aging and SOA differ  
433 markedly between the heating rate and the downward flux. The cooling effect of the  
434 atmosphere ( $\sim 1 \text{ km}$ ) is seen over northern China ( $30 - 40^{\circ}\text{N}$ ) and over the Asian continent  
435 (Fig. 9g), whereas the negative radiative impact at the surface is seen over southern China  
436 ( $20 - 30^{\circ}\text{N}$ ) and over the western Pacific (Fig. 9h). Because the impact of each process  
437 on each radiative parameter has a large latitudinal dependence (Fig. 9c-f), the total effects

438 also have large latitudinal dependences. Positive and negative impacts are seen for both  
439 the heating rate and the downward flux, although the warming effect at around 25°N (Fig.  
440 9g) and the positive downward flux over northern China (Fig. 9h) are not very large.

441 Aerosol optical and radiative parameters in the M08\_SN, M06\_SN, and  
442 M04\_SN simulations are generally similar to those in the benchmark M10\_SN simulation,  
443 although the performance deteriorates as the number of BC mixing state bins is decreased.  
444 The M06\_SN and M04\_SN simulations can explain 70 – 85% and 65 – 75% of the total  
445 BC mixing state effect (the difference in aerosol optical and radiative parameters between  
446 the M10\_SN and M01\_SN simulations; Table 4). These results suggest that the  
447 simulations with 4 or more mixing state bins could generally explain the actual BC mixing  
448 state effect reasonably well in terms of aerosol optical and radiative parameters in the  
449 boundary layer.

450 The NPF sensitivity of all the optical and radiative parameters examined in this  
451 study is small (Table 4). However, because NPF increases CCN concentrations (Sect.  
452 3.3), this process may be of great importance in terms of the indirect effects of aerosols.  
453 SOA may also be important in estimating indirect effects because of the large sensitivity  
454 of SOA to CCN concentrations (Sect. 3.3). A simulation with a higher grid resolution  
455 is necessary to resolve fine-scale clouds and to evaluate indirect effects accurately. This  
456 type of study will be important in the future, but it is beyond the scope of this study.

457 The sensitivities of the mass, number, size distribution, and optical and radiative  
458 parameters of aerosols to NPF, BC aging, and SOA processes (discussed in Sect. 3.3 and  
459 3.4) are shown in Fig. 10. The impact (positive or negative) and the relative importance  
460 of each process markedly differ between the parameters. We calculated these

461 complicated responses for the first time using a detailed aerosol model that could  
462 explicitly and simultaneously represent important physical and chemical processes of  
463 aerosols. Because these responses have large spatial and temporal dependences, further  
464 applications are needed to understand more thoroughly the importance of individual  
465 aerosol processes.

466

#### 467 **4. Summary and conclusions**

468 We developed an aerosol module, Aerosol Two-dimensional bin module for  
469 foRmation and Aging Simulation (ATRAS), and implemented it into the WRF-  
470 chem/MOSAIC model. This module can represent important physical and chemical  
471 processes (NPF, BC aging, and SOA) that control the number concentrations, size  
472 distributions, and mixing states of aerosols in the atmosphere. ATRAS uses a total of  
473 128 aerosol bins (at maximum). A two-dimensional bin representation is used for  
474 particles with dry diameters from 40 nm to 10  $\mu\text{m}$  in diameter to resolve both aerosol  
475 sizes and BC mixing states ( $12 \times 10$  bins). Particles with diameters from 1 to 40 nm are  
476 resolved using additional 8 size bins to calculate NPF.

477 We applied ATRAS-MOSAIC to the East Asian region in the spring of 2009,  
478 where and when aerosol mass and number concentrations and their spatial and temporal  
479 variations were evaluated in detail by both aircraft and surface measurements. The  
480 performance of ATRAS-MOSAIC was similar to or better than that of our previous WRF-  
481 chem/MOSAIC simulations.

482 We examined the sensitivity of the mass, number, size distributions, and optical  
483 and radiative parameters of aerosols to NPF, BC aging (resolution of BC mixing state),

484 and SOA processes by comparing the simulation results with (128 bins) and without (12  
485 bins, assuming internally-mixed particles) these processes. SOA processes increased  
486 PM<sub>2.5</sub> and OA mass concentrations by 25% and 300%, respectively (period- and domain-  
487 averaged values in the boundary layer). BC mass concentrations were increased by 10  
488 – 15% by the treatment of the BC mixing state (Fig. 10).

489 CCN<sub>1.0</sub> and CCN<sub>0.1</sub> concentrations in the boundary layer were increased by 18%  
490 and 16%, respectively, by both NPF and SOA processes. We found a clear north-south  
491 contrast between the impacts of NPF and SOA processes on CCN concentrations. NPF  
492 increased CCN concentrations at higher supersaturations (smaller particles) over northern  
493 East Asia, whereas SOA increased CCN concentrations at lower supersaturations (larger  
494 particles) over southern East Asia (Fig. 10). These processes will be important for the  
495 evaluation of the indirect effects of aerosols.

496 The detailed treatment of BC mixing state reduced the absorption coefficient  
497 because the absorption enhancement (due to the lens effect) was overestimated by a factor  
498 of 2 in the simulation without the treatment of the BC mixing state (i.e., when internally  
499 mixing of BC particles is assumed) (Fig. 10). The absorption enhancement ratio by the  
500 lens effect was about 60% in our simulation over East Asia. SOA processes increased  
501 both scattering and absorption coefficients (by the lens effect) (Fig. 10). The  
502 contribution of SOA processes to the total absorption enhancement was estimated to be  
503 20% over northern East Asia and 20 – 40% over southern East Asia.

504 BC aging processes decreased the heating rate at 1 km by 0.3 K d<sup>-1</sup> and increased  
505 the downward flux at the surface by 5 W m<sup>-2</sup>, mainly over northern China, where BC  
506 concentrations were high. SOA processes increased the heating rate at 1 km by 0.1 K d<sup>-1</sup>

507 <sup>1</sup> and decreased the downward flux at the surface by  $15 \text{ W m}^{-2}$ , mainly over southern  
508 China, where OA concentrations were high. As a result, the spatial distributions of the  
509 combined effects of BC aging and SOA processes differ substantially between the heating  
510 rate and the downward flux.

511 Sensitivity simulations showed that the simulations with 4 or more mixing state  
512 bins could generally explain the actual BC mixing state effect reasonably well in terms of  
513 BC mass concentrations and aerosol optical and radiative parameters. Therefore,  
514 simulations with 4 mixing state bins may be reasonable for global applications by  
515 considering the balance between accuracy and computational cost. On the other hand,  
516 as the results are improved (approaching to the simulation with 10 mixing state bins) with  
517 increasing the number of mixing state bins, simulations with sufficient number of mixing  
518 state bins may be necessary when we focus on the detailed information of BC mixing  
519 state.

520 For further improvements of our model, a nucleation parameterization  
521 considering the contribution of organic vapors to nucleation (Metzger et al., 2010) may  
522 be useful. Low volatile organic vapors, brown carbon, and OA formation in the aerosol  
523 phase will also be key factors for the model improvement of OA formation and its  
524 radiative effect (Liu et al., 2012; Feng et al., 2013). Including the formation of ice nuclei  
525 is another important step for studies on aerosol-cloud interactions. Extending BC  
526 mixing state treatments to dust particles may be the key to more realistic simulations of  
527 ice nuclei concentrations and their formation pathways.

528 ATRAS-MOSAIC has the potential to be a benchmark module for aerosol  
529 microphysical and chemical processes. The module can be used to understand which

530 processes and parameters should be represented in detail and which ones can be simplified  
531 in predicting the mass, number, size distributions, and optical and radiative parameters of  
532 aerosols. The module can also be used to examine complicated interactions between  
533 aerosol processes, such as the impact of SOA on NPF and on BC aging and removal.  
534 The detailed aerosol model will be a useful tool for understanding the complicated and  
535 nonlinear climatic responses of aerosol processes to the change in meteorological  
536 conditions and emissions of chemical species in the future.

537

538 **Acknowledgments.**

539 This work was supported by the Ministry of Education, Culture, Sports, Science, and  
540 Technology and the Japan Society for the Promotion of Science (MEXT/JSPS)  
541 KAKENHI grant numbers 26740014 and 23221001. This work was also supported by  
542 the strategic international cooperative program of the Japan Science and Technology  
543 Agency, the global environment research fund of the Ministry of the Environment, Japan  
544 (2A-1101), and the Alliance for Global Sustainability project of the University of Tokyo.  
545 The authors thank Nobuhiro Moteki (University of Tokyo), Nobuyuki Takegawa  
546 (University of Tokyo), Akinori Takami (National Institute for Environmental Studies),  
547 Yugo Kanaya (Japan Agency for Marine-Earth Science and Technology), Soonchang  
548 Yoon (Seoul National University), and Sang-Woo Kim (Seoul National University) for  
549 providing the measurement data during the A-FORCE campaign. For some of the  
550 simulations, we used the supercomputer systems at the University of Tokyo and Japan  
551 Agency for Marine-Earth Science and Technology. J. D. Fast was supported by the U.S.  
552 Department of Energy (DOE) Atmospheric System Research (ASR) program under  
553 Contract DE-AC06-76RLO 1830 at PNNL. PNNL is operated for the U.S. DOE by  
554 Battelle Memorial Institute.

555

556

557    **References.**

- 558    Abdul-Razzak, H. and Ghan, S. J.: A parameterization of aerosol activation: 2. Multiple  
559    aerosol types, *J. Geophys. Res.*, 105(D5), 6837–6844, doi:10.1029/1999JD901161,  
560    2000.
- 561    Aquila, V., Hendricks, J., Lauer, A., Riemer, N., Vogel, H., Baumgardner, D., Minikin,  
562    A., Petzold, A., Schwarz, J. P., Spackman, J. R., Weinzierl, B., Righi, M., and  
563    Dall'Amico, M.: MADE-in: a new aerosol microphysics submodel for global  
564    simulation of insoluble particles and their mixing state, *Geosci. Model Dev.*, 4, 325–  
565    355, 2011.
- 566    Bohren, C. F. and Huffman, D. R.: *Absorption and Scattering of Light by Small Particles*,  
567    530 pp, John Wiley, Hoboken, N. J., 1998.
- 568    Bond, T. C., Habib, G., and Bergstrom, R. W.: Limitations in the enhancement of visible  
569    light absorption due to mixing state, *J. Geophys. Res.*, 111, D20211,  
570    doi:10.1029/2006JD007315, 2006.
- 571    Bond, T. C., Doherty, S. J., Fahey, D. W., Forster, P. M., Berntsen, T., DeAngelo, B. J.,  
572    Flanner, M. G., Ghan, S., Kärcher, B., Koch, D., Kinne, S., Kondo, Y., Quinn, P.  
573    K., Sarofim, M. C., Schultz, M. G., Schulz, M., Venkataraman, C., Zhang, H.,  
574    Zhang, S., Bellouin, N., Guttikunda, S. K., Hopke, P. K., Jacobson, M. Z., Kaiser,  
575    J. W., Klimont, Z., Lohmann, U., Schwarz, J. P., Shindell, D., Storelvmo, T.,  
576    Warren, S. G., and Zender, C. S.: Bounding the role of black carbon in the climate  
577    system: A scientific assessment, *J. Geophys. Res. Atmos.*, 118, 5380 – 5552,  
578    doi:10.1002/jgrd.50171, 2013.
- 579    Carter, W. P. L.: Documentation of the SAPRC-99 Chemical Mechanism for VOC

580        Reactivity Assessment, Report to the California Air Resources Board. College of  
581        Engineering, Center for Environmental Research and Technology, University of  
582        California at Riverside, CA. Contracts 92–329 and 95–308, available at:  
583        <http://www.cert.ucr.edu/~carter/reactdat.htm>, 2000.

584        Donahue, N. M., Robinson, A. L., Stanier, C. O., and Pandis, S. N.: Coupled partitioning,  
585        dilution, and chemical aging of semivolatile organics, Environ. Sci. Technol., 40,  
586        2635 – 2643, 2006.

587        Easter, R. C., Ghan, S. J., Zhang, Y., Saylor, R. D., Chapman, E. G., Laulainen, N. S.,  
588        Abdul-Razzak, H., Leung, L. R., Bian, X. and Zaveri, R. A.: MIRAGE: Model  
589        description and evaluation of aerosols and trace gases, J. Geophys. Res., 109,  
590        D20210, doi:10.1029/2004JD004571, 2004.

591        Fahey, K. M. and Pandis, S. N.: Optimizing model performance: Variable size resolution  
592        in cloud chemistry modeling, Atmos. Environ., 35, 4471– 4478, 2001.

593        Fast, J. D., Gustafson Jr., W. I., Easter, R. C., Zaveri, R. A., Barnard, J. C., Chapman, E.  
594        G., Grell, G. A., and Peckham, S. E.: Evolution of ozone, particulates, and aerosol  
595        direct radiative forcing in the vicinity of Houston using a fully coupled  
596        meteorology-chemistry-aerosol model, J. Geophys. Res., 111, D21305,  
597        doi:10.1029/2005JD006721, 2006.

598        Feng, Y., Ramanathan, V., and Kotamarthi, V. R.: Brown carbon: a significant  
599        atmospheric absorber of solar radiation, Atmos. Chem. Phys., 13, 8607 – 8621, 2013.

600        Ghan, S. J., Abdul-Razzak, H., Nenes, A., Ming, Y., Liu, X., Ovchinnikov, M., Shipway,  
601        B., Meskhidze, N., Xu, J., and Shi, X.: Droplet nucleation: Physically-based  
602        parameterizations and comparative evaluation, J. Adv. Model. Earth Syst., 3,

- 603 M10001, 33 pp, 2011.
- 604 Grell, G. A., Peckham, S. E., Schmitz, R., McKeen, S. A., Frost, G., Skamarock, W. C.,  
605 and Eder, B: Fully coupled “online” chemistry within the WRF model, *Atmos.*  
606 *Environ.*, 39, 6957 – 6975, 2005.
- 607 Guenther, A., Karl, T., Harley, P., Wiedinmyer, C., Palmer, P. I., and Geron, C.: Estimates  
608 of global terrestrial isoprene emissions using MEGAN (Model of Emissions of  
609 Gases and Aerosols from Nature), *Atmos. Chem. Phys.*, 6, 3181 – 3210, 2006.
- 610 Hallquist, M., Wenger, J. C., Baltensperger, U., Rudich, Y., Simpson, D., Claeys, M.,  
611 Dommen, J., Donahue, N. M., George, C., Goldstein, A. H., Hamilton, J. F.,  
612 Herrmann, H., Hoffmann, T., Iinuma, Y., Jang, M., Jenkin, M. E., Jimenez, J. L.,  
613 Kiendler-Scharr, A., Maenhaut, W., McFiggans, G., Mental, F., Monod, A., Pfevôt,  
614 A. S. H., Seinfeld, J. H., Surratt, J. D., Szmigielski, R., and Wildt, J.: The formation,  
615 properties and impact of secondary organic aerosol: current and emerging issues,  
616 *Atmos. Chem. Phys.*, 9, 5155 – 5236, 2009.
- 617 Heald, C. L., Jacob, D. J., Park, R. J., Russell, L. M., Huebert, B. J., Seinfeld, J. H., Liao,  
618 H., and Weber, R. J.: A large organic aerosol source in the free troposphere missing  
619 from current models, *Geophys. Res. Lett.*, 32, L18809, doi:10.1029/2005GL023831,  
620 2005.
- 621 Heald, C. L., Coe, H., Jimenez, J. L., Weber, R. J., Bahreini, R., Middlebrook, A. M.,  
622 Russell, L. M., Jolley, M., Fu, T.-M., Allan, J. D., Bower, K. N., Capes, G., Crosier,  
623 J., Morgan, W. T., Robinson, N. H., Williams, P. I., Cubison, M. J., DeCarlo, P. F.,  
624 and Dunlea, E. J.: Exploring the vertical profile of atmospheric organic aerosol:  
625 comparing 17 aircraft field campaigns with a global model, *Atmos. Chem. Phys.*,

- 626 11, 12673 – 12696, 2011.
- 627 IPCC: Summary for Policymakers. In: Climate Change 2013: The Physical Science Basis.  
628 Contribution of Working Group I to the Fifth Assessment Report of the  
629 Intergovernmental Panel on Climate Change [Stocker, T.F., Qin, D, Plattner, G.-K.,  
630 Tignor, M., Allen, S. K., Boschung, J., Nauels, A., Xia, Y., Bex, V., and Midgley,  
631 P. M. (eds.)], Cambridge University Press, Cambridge, United Kingdom and New  
632 York, NY, USA, 2013.
- 633 Jacobson, M. Z., Turco, R. P., Jensen, E. J., and Toon, O. B.: Modeling coagulation  
634 among particles of different composition and size, *Atmos. Environ.*, 28, 1327–1338,  
635 1994.
- 636 Jacobson, M. Z.: Development and application of a new air pollution modeling system—  
637 II. Aerosol module structure and design, *Atmos. Environ.*, 31, 131–144, 1997.
- 638 Jacobson, M. Z.: A physically-based treatment of elemental carbon optics: Implications  
639 for global direct forcing of aerosols, *Geophys. Res. Lett.*, 27(2), 217–220,  
640 doi:10.1029/1999GL010968, 2000.
- 641 Jacobson, M. Z: Strong radiative heating due to the mixing state of black carbon in  
642 atmospheric aerosols, *Nature*, 409, 695–697, 2001.
- 643 Jimenez, J. L., Canagaratna, M. R., Donahue, N. M., et al.: Evolution of organic aerosols  
644 in the atmosphere, *Science*, 326, 1525 – 1529, 2009.
- 645 Kanakidou, M., Seinfeld, J. H., Pandis, S. N., Barnes, I., Dentener, F. J., Facchini, M. C.,  
646 Van Dingenen, R., Ervens, B., Nenes, A., Nielsen, C. J., Swietlicki, E., Putaud, J.  
647 P., Balkanski, Y., Fuzzi, S., Horth, J., Moortgat, G. K., Winterhalter, R., Myhre, C,  
648 E. L., Tsigaridis, K., Vignati, E., Stephanou, E. G., and Wilson, J.: Organic aerosol

- 649 and global climate modeling: A review, *Atmos. Chem. Phys.*, 5, 1053– 1123, 2005.
- 650 Kanaya, Y., Taketani, F., Komazaki, Y., Liu, X., Kondo, Y., Sahu, L. K., Irie, H., and
- 651 Takashima, H.: Comparison of black carbon mass concentrations observed by
- 652 Multi-Angle Absorption Photometer (MAAP) and Continuous Soot-Monitoring
- 653 System (COSMOS) on Fukue Island and in Tokyo, Japan, *Aerosol Sci. Technol.*,
- 654 47(1), 1–10, 2013.
- 655 Kondo, Y., Sahu, L., Moteki, N., Khan, F., Takegawa, N., Liu, X., Koike, M., and
- 656 Miyakawa, T.: Consistency and traceability of black carbon measurements made by
- 657 laser-induced incandescence, thermal-optical transmittance, and filter-based photo-
- 658 absorption techniques, *Aerosol Sci. Technol.*, 45, 295–312, 2011.
- 659 Koo, B., Ansari, A. S., and Pandis, S. N.: Integrated approaches to modeling the organic
- 660 and inorganic atmospheric aerosol components, *Atmos. Environ.*, 37, 4757 – 4768,
- 661 2003.
- 662 Korhola, T., Kokkola, H., Korhonen, H., Partanen, A.-I., Laaksonen, A., Lehtinen, K. E.
- 663 J., and Romakkaniemi, S.: Reallocation in modal aerosol models: impacts on
- 664 predicting aerosol radiative effects, *Geosci. Model Dev.*, 7, 161-174, 2014.
- 665 Kuang, C., McMurry, P. H., McCormick, A. V., and Eisele, F. L.: Dependence of
- 666 nucleation rates on sulfuric acid vapor concentration in diverse atmospheric
- 667 locations, *J. Geophys. Res.*, 113, D10209, doi:10.1029/2007JD009253, 2008.
- 668 Kulmala, M., Pirjola, L., and Mäkelä, J. M.: Stable sulphate clusters as a source of new
- 669 atmospheric particles, *Nature*, 404, 66–69, 2000.
- 670 Kulmala, M., Vehkamäki, H., Petäjä, T., Dal Maso, M., Lauri, A., Kerminen, V.-M.,
- 671 Birmili, W., and McMurry, P. H.: Formation and growth rates of ultrafine

- 672 atmospheric particles: A review of observations, *J. Aerosol Sci.*, 35, 143–176, 2004.
- 673 Kulmala, M., Lehtinen, K. E. J., and Laaksonen, A.: Cluster activation theory as an  
674 explanation of the linear dependence between formation rate of 3 nm particles and  
675 sulphuric acid concentration, *Atmos. Chem. Phys.*, 6, 787–793, 2006.
- 676 Kulmala, M., Riipinen, I., Sipilä, M., Manninen, H. E., Petäjä, T., Junninen, H., Dal Maso,  
677 Mordas, G., Mirme, A., Vana, M., Hirsikko, A., Laakso, L., Harrison, R. M.,  
678 Hanson, I., Leung, C., Lehtinen, K. E. J., and Kerminen, V.-M.: Toward direct  
679 measurement of atmospheric nucleation, *Science*, 318, 89–92, 2007.
- 680 Liu, J., Horowitz, L. W., Fan, S., Carlton, A. G., and Levy II, H.: Global in-cloud  
681 production of secondary organic aerosols: Implementation of a detailed chemical  
682 mechanism in the GFDL atmospheric model AM3, *J. Geophys. Res.*, 117, D15303,  
683 doi:10.1029/2012JD017838, 2012.
- 684 Lohmann, U. and Feichter, J.: Global indirect aerosol effects: A review, *Atmos. Chem.  
685 Phys.*, 5, 715–737, 2005.
- 686 Makkonen, R., Asmi, A., Korhonen, H., Kokkola, H., Järvenoja, S., Räisänen, P.,  
687 Lehtinen, K. E. J., Laaksonen, A., Kerminen, V.-M., Järvinen, H., Lohmann, U.,  
688 Bennartz, R., Feichter, J., and Kulmala, M.: Sensitivity of aerosol concentrations  
689 and cloud properties to nucleation and secondary organic distribution in ECHAM5-  
690 HAM global circulation model, *Atmos. Chem. Phys.*, 9, 1747–1766, 2009.
- 691 Makkonen, R., Asmi, A., Kerminen, V.-M., Boy, M., Arneth, A., Hari, P., and Kulmala,  
692 M.: Air pollution control and decreasing new particle formation lead to strong  
693 climate warming, *Atmos. Chem. Phys.*, 12, 1515 – 1524, 2012.
- 694 Matsui, H., Koike, M. Takegawa, N. Kondo, Y., Griffin, R. J., Miyazaki, Y., Yokouchi,

- 695 Y., and Ohara, T.: Secondary organic aerosol formation in urban air: Temporal  
696 variations and possible contributions from unidentified hydrocarbons, *J. Geophys.*  
697 *Res.*, 114, D04201, doi:10.1029/2008JD010164, 2009a.
- 698 Matsui, H., Koike, M., Kondo, Y., Takegawa, N., Kita, K., Miyazaki, Y., Hu, M., Chang,  
699 S.-Y., Blake, D. R., Fast, J. D., Zaveri, R. A., Streets, D. G., Zhang, Q., and Zhu, T:  
700 Spatial and temporal variations of aerosols around Beijing in summer 2006: Model  
701 evaluation and source apportionment, *J. Geophys. Res.*, 114, D00G13,  
702 doi:10.1029/2008JD010906, 2009b.
- 703 Matsui, H., Koike, M., Kondo, Y., Takegawa, N., Fast, J. D., Pöschl, U., Garland, R. M.,  
704 Andreae, M. O., Wiedensohler, A., Sugimoto, N., and Zhu, T.: Spatial and temporal  
705 variations of aerosols around Beijing in summer 2006: 2. Local and column aerosol  
706 optical properties, *J. Geophys. Res.*, 115, D22207, doi:10.1029/2010JD013895,  
707 2010.
- 708 Matsui, H., Koike, M., Kondo, Y., Takegawa, N., Wiedensohler, A., Fast, J. D., and  
709 Zaveri, R. A.: Impact of new particle formation on the concentrations of aerosols  
710 and cloud condensation nuclei around Beijing, *J. Geophys. Res.*, 116, D19208,  
711 doi:10.1029/2011JD016025, 2011.
- 712 Matsui, H., Koike, M., Kondo, Y., Moteki, N., Fast, J. D., and Zaveri, R. A.: Development  
713 and validation of a black carbon mixing state resolved three-dimensional model:  
714 Aging processes and radiative impact, *J. Geophys. Res. Atmos.*, 118,  
715 doi:10.1029/2012JD018446, 2013a.
- 716 Matsui, H., Koike, M., Takegawa, N., Kondo, Y., Takami, A., Takamura, T., Yoon, S.,  
717 Kim, S.-W., Lim, H.-C., and Fast, J. D.: Spatial and temporal variations of new

- 718 particle formation in East Asia using an NPF-explicit WRF-chem model: North-  
719 south contrast in new particle formation frequency, *J. Geophys. Res. Atmos.*, 118,  
720 doi:10.1002/jgrd.50821, 2013c.
- 721 Matsui, H., K. Koike, Kondo, Y., Takami, A., Fast, J. D., Kanaya, Y., and Takigawa, M.:  
722 Volatility basis-set approach simulation of organic aerosol formation in East Asia:  
723 Implications for anthropogenic-biogenic interaction and controllable amounts,  
724 *Atmos. Chem. Phys. Discuss.*, 14, 6203 – 6260, 2014.
- 725 Merikanto, J., Spracklen, D. V., Mann, G. W., Pickering, S. J., and Carslaw, K. S.: Impact  
726 of nucleation on global CCN, *Atmos. Chem. Phys.*, 9, 8601–8616, 2009.
- 727 Metzger, A., Verheggen, B., Dommen, J., Duplissy, J., Prevot, A. S. H., Weingartner, E.,  
728 Riipinen, I., Kulmala, M., Spracklen, D. V., Carslaw, K. S., and Baltensperger, U.:  
729 Evidence for the role of organics in aerosol particle formation under atmospheric  
730 conditions, *Proc. Natl. Acad. Sci. USA*, 107, 6646 – 6651, 2010.
- 731 Moteki, N. and Kondo, Y.: Effects of mixing state on black carbon measurements by  
732 laser-induced incandescence, *Aerosol Sci. Technol.*, 41(4), 398–417, 2007.
- 733 Moteki, N. and Kondo, Y.: Dependence of laser-induced incandescence on physical  
734 properties of black carbon aerosols: Measurements and theoretical interpretation,  
735 *Aerosol Sci. Technol.*, 44(8), 663–675, 2010.
- 736 Moteki, N., Kondo, Y., Miyazaki, Y., Takegawa, N., Komazaki, Y., Kurata, G., Shirai,  
737 T., Blake, D. R., Miyakawa, T., and Koike, M.: Evolution of mixing state of black  
738 carbon particles: Aircraft measurements over the western Pacific in March 2004,  
739 *Geophys. Res. Lett.*, 34, L11803, doi:10.1029/2006GL028943, 2007.
- 740 Moteki, N., Kondo, Y., Oshima, N., Takegawa, N., Koike, M., Kita, K., Matsui, H., and

- 741 Kajino, M.: Size dependence of wet removal of black carbon aerosols during  
742 transport from the boundary layer to the free troposphere, *Geophys. Res. Lett.*, 39,  
743 L13802, doi:10.1029/2012GL052034, 2012.
- 744 Oshima, N., Koike, M., Zhang, Y., and Kondo, Y.: Aging of black carbon in outflow from  
745 anthropogenic sources using a mixing state resolved model: 2. Aerosol optical  
746 properties and cloud condensation nuclei activities, *J. Geophys. Res.*, 114, D18202,  
747 doi:10.1029/2008JD011681, 2009.
- 748 Oshima, N., Kondo, Y., Moteki, N., Takegawa, N., Koike, M., Kita, K., Matsui, H.,  
749 Kajino, M., Nakamura, H., Jung, J. S., and Kim, Y. J.: Wet removal of black carbon  
750 in Asian outflow: Aerosol Radiative Forcing in East Asia (A-FORCE) aircraft  
751 campaign, *J. Geophys. Res.*, 117, D03204, doi:10.1029/2011JD016552, 2012.
- 752 Ramanathan, V., Crutzen, P. J., Kiehl, J. T., and Rosenfeld, D.: Aerosols, climate, and  
753 the hydrological cycle, *Science*, 294(5549), 2119–2124, 2001.
- 754 Reddington, C. L., Carslaw, K. S., Spracklen, D. V., Frontoso, M. G., Collins, L.,  
755 Merikanto, J., Minikin, A., Hamburger, T., Coe, H., and Kulmala, M.: Primary  
756 versus secondary contributions to particle number concentrations in the European  
757 boundary layer, *Atmos. Chem. Phys.*, 11, 12,007–12,036, 2011.
- 758 Schell, B., Ackermann, I. J., Hass, H., Binkowski, F. S., and Ebel, A.: Modeling the  
759 formation of secondary organic aerosol within a comprehensive air quality model  
760 system, *J. Geophys. Res.*, 106, 28275–28293, doi:10.1029/2001JD000384, 2001.
- 761 Shrivastava, M., Fast, J., Easter, R., Gustafson Jr., W. I., Zaveri, R. A., Jimenez, J. L.,  
762 Saide, P., and Hodzic, A.: Modeling organic aerosols in a megacity: comparison of  
763 simple and complex representations of the volatility basis set approach, *Atmos.*

764 Chem. Phys., 11, 6639 – 6662, 2011.

765 Simmel, M. and Wurzler, S.: Condensation and activation in sectional cloud  
766 microphysical models, Atmos. Res., 80, 218–236, 2006.

767 Skamarock, W. C., Klemp, J. B., Dudhia, J., Gill, D. O., Barker, D. M., Wang, W., and  
768 Powers, J. G.: A description of the advanced research WRF version 3, NCAR Tech.  
769 Note, NCAR/TN-475+STR, Natl. Cent. Atmos. Res., Boulder, Colo, 2008.

770 Spracklen, D. V., Carslaw, K. S., Kulmala, M., Kerminen, V.-M., Mann, G. W., and Sihto,  
771 S.-L.: The contribution of boundary layer nucleation events to total particle  
772 concentrations on regional and global scales, Atmos. Chem. Phys., 6, 5631–5648,  
773 2006.

774 Spracklen, D. V., Carslaw, K. S., Kulmala, M., Kerminen, V.-M., Sihto, S.-L., Riipinen,  
775 I., Merikanto, J., Mann, G. W., Chipperfield, M. P., Wiedensohler, A., Birmili, W.,  
776 and Lihavainen, H.: Contribution of particle formation to global cloud condensation  
777 nuclei concentrations, Geophys. Res. Lett., 35, L06808,  
778 doi:10.1029/2007GL033038, 2008.

779 Spracklen, D. V., Carslaw, K. S., Merikanto, J., Mann, G. W., Reddington, C. L.,  
780 Pickering, S., Ogren, J. A., Andrews, E., Baltensperger, U., Weingartner, E., Boy,  
781 N., Kulmala, M., Laakso, L., Lihavainen, H., Kivekäs, N., Komppula, M.,  
782 Mihalopoulos, N., Kouvarakis, G., Jennings, S. G., O'Dowd, C., Birmili, W.,  
783 Wiedensohler, A., Weller, R., Gras, J., Laj, P., Sellegri, K., Bonn, B., Krejci, R.,  
784 Laaksonen, A., Hamed, A., Minikin, A., Harrison, R., M., Talbot, R., and Sun, J.:  
785 Explaining global surface aerosol number concentrations in terms of primary  
786 emissions and particle formation, Atmos. Chem. Phys., 10, 4775–4793, 2010.

- 787 Spracklen, D. V., Jimenez, J. L., Carslaw, K. S., Worsnop, D. R., Evans, M. J., Mann, G.  
788 W., Zhang, Q., Canagaratna, M. R., Allan, J., Coe, H., McFiggans, G., Rap, A., and  
789 Forster, P.: Aerosol mass spectrometer constraint on the global secondary organic  
790 aerosol budget, *Atmos. Chem. Phys.*, 11, 12109 – 12136, 2011.
- 791 Stier, P., Seinfeld, J. H., Kinne, S., Feichter, J., and Boucher, O.: Impact of nonabsorbing  
792 anthropogenic aerosols on clear-sky atmospheric absorption, *J. Geophys. Res.*, 111,  
793 D18201, doi:10.1029/2006JD007147, 2006.
- 794 Streets, D. G., Bond, T. C., Carmichael, G. R., Fernandes, S. D., Fu, Q., He, D., Klimont,  
795 Z., Nelson, S. M., Tsai, N. Y., Wang, M. Q., Woo, J.-H., and Yarber, K. F.: An  
796 inventory of gaseous and primary aerosol emissions in Asia in the year 2000, *J.*  
797 *Geophys. Res.*, 108(D21), 8809, doi:10.1029/2002JD003093, 2003.
- 798 Takami, A., Miyoshi, T., Shimono, A., and Hatakeyama, S.: Chemical composition of  
799 fine aerosol measured by AMS at Fukue Island, Japan, during APEX period, *Atmos.*  
800 *Environ.*, 39, 4913–4924, 2005.
- 801 Takami, A., Miyoshi, T., Shimono, A., Kaneyasu, N., Kato, S., Kajii, Y., and Hatakeyama,  
802 S.: Transport of anthropogenic aerosols from Asia and subsequent chemical  
803 transformation, *J. Geophys. Res.*, 112, D22S31, doi:10.1029/2006JD008120, 2007.
- 804 Takegawa, N., Moteki, N., Koike, M., Oshima, N., and Kondo, Y.: Condensation particle  
805 counters combined with a low-pressure impactor for fast measurement of mode-  
806 segregated aerosol number concentration, *Aerosol Sci. Technol.*, 47, 1059–1065,  
807 2013.
- 808 Tsimpidi, A. P., Karydis, V. A., Zavala, M., Lei, W., Molina, L., Ulbrich, I. M., Jimenez,  
809 J. L., and Pandis, S. N.: Evaluation of the volatility basis-set approach for the

810 simulation of organic aerosol formation in the Mexico City metropolitan area,  
811 Atmos. Chem. Phys., 10, 525 – 546, 2010.

812 van der Werf, G. R., Randerson, J. T., Giglio, L., Collatz, G. J., Mu, M., Kasibhatla, P.  
813 S., Morton, D. C., DeFries, R. S., Jin, Y., and van Leeuwen, T. T.: Global fire  
814 emissions and the contribution of deforestation, savanna, forest, agricultural, and  
815 peat fires (1997 – 2009), Atmos. Chem. Phys., 10, 11707 – 11735, 2010.

816 Wexler, A. S., Lurmann, F. W., and Seinfeld, J. H.: Modelling urban and regional aerosols.  
817 Part I: Model development, Atmos. Environ., 28, 531–546, 1994.

818 Yu, F., Luo, G., and Ma, X.: Regional and global modeling of aerosol optical properties  
819 with a size, composition, and mixing state resolved particle microphysical model,  
820 Atmos. Chem. Phys., 12, 5719 – 5736, 2012.

821 Zaveri, R. A., Easter, R. C., and Wexler, A. S.: A new method for multicomponent  
822 activity coefficients of electrolytes in aqueous atmospheric aerosols, J. Geophys.  
823 Res., 110, D02201, doi:10.1029/2004JD004681, 2005a.

824 Zaveri, R. A., Easter, R. C., and Peters, L. K.: A computationally efficient  
825 Multicomponent Equilibrium Solver for Aerosols (MESA), J. Geophys. Res., 110,  
826 D24203, doi:10.1029/2004JD005618, 2005b.

827 Zaveri, R. A., Easter, R. C., Fast, J. D., and Peters, L. K.: Model for Simulating Aerosol  
828 Interactions and Chemistry (MOSAIC), J. Geophys. Res., 113, D13204,  
829 doi:10.1029/2007JD008782, 2008.

830 Zhang, Q., Jimenez, J. L., Canagaratna, M. R. et al.: Ubiquity and dominance of  
831 oxygenated species in organic aerosols in anthropogenically influenced Northern  
832 Hemisphere midlatitudes, Geophys. Res. Lett., 34, L13801,

833                   doi:10.1029/2007GL029979, 2007.

834

835

836

837   **Author's addresses**

838   J. D. Fast, Atmospheric Science and Global Change Division, Pacific Northwest National  
839       Laboratory, MSINK9-30, P.O. Box 999, Richland, WA 99352, USA.  
840       (jerome.fast@pnnl.gov)

841   M. Koike and Y. Kondo, Department of Earth and Planetary Science, Graduate School of  
842       Science, The University of Tokyo, Hongo 7-3-1, Bunkyo-ku, Tokyo, 113-0033,  
843       Japan. (koike@eps.s.u-tokyo.ac.jp, kondo@eps.s.u-tokyo.ac.jp)

844   H. Matsui and M. Takigawa, Japan Agency for Marine-Earth Science and Technology,  
845       3173-25, Showa-machi, Kanazawa-ku, Yokohama, Kanagawa, 236-0001, Japan.  
846       (matsui@jamstec.go.jp, takigawa@jamstec.go.jp)

847

848

849    **Figure captions**

850    Fig. 1. Aerosol bin representation used in the ATRAS module. Particles with dry  
851    diameters from 40 nm to 10  $\mu\text{m}$  are placed into two-dimensional bins. One  
852    dimension is aerosol dry diameter (12 bins from 40 nm to 10  $\mu\text{m}$ ), and the other  
853    dimension is the fraction of BC mass relative to total aerosol mass concentration  
854    under dry condition (10 bins; pure-BC particles, BC-free particles, and 8  
855    different internally-mixed BC particles). The particles with dry diameters from  
856    1 to 40 nm are divided into 8 size bins to calculate NPF.

857    Fig. 2. (a) Simulation domain used in this study. The simulations are conducted from  
858    21 March to 26 April 2009 with horizontal resolutions of 360 km (outer domain,  
859    orange) and 120 km (inner domain). (b) The locations of surface measurements  
860    at the Fukue and Hedo sites and the flight tracks during the A-FORCE aircraft  
861    campaign, which are used to validate the model simulations in this study.

862    Fig. 3. Comparison of the model simulation results with the observed average mass  
863    concentrations of BC ( $M_{\text{BC}}$ ), sulfate ( $M_{\text{SO}_4}$ ), and organic aerosols ( $M_{\text{OA}}$ ), the  
864    volume concentration of light scattering particles ( $V_{\text{LSP}}$ ), the shell-to-core  
865    diameter ratio at a BC core diameter of 200 nm (SC ratio), and the number  
866    concentration of Aitken-mode particles (10 – 130 nm) (CN). The simulated  
867    aerosol concentrations are chosen from the horizontal and vertical grids closest  
868    to each site (for surface measurements at Fukue and Hedo) or flight track (for  
869    aircraft measurements during A-FORCE).

870    Fig. 4. The period-averaged PM<sub>2.5</sub> (a) M10\_SN and (b) M01 runs, CCN concentrations  
871    at supersaturations of 1% (CCN<sub>1.0</sub>) (c) M10\_SN and (d) M01 runs, and CCN

872 concentrations at supersaturations of 0.1% (CCN<sub>0.1</sub>) (e) M10\_SN and (f) M01  
873 runs at a sigma level of 0.895 (~1 km). Period-averaged values are calculated  
874 using the data at 12:00 local time (03:00 UTC) between 24 March and 26 April.

875 Fig. 5. The period-averaged dCCN concentrations at a sigma level of 0.895 (~1 km).  
876 dCCN is defined as the difference in the CCN concentration between M01\_N  
877 and M01 (left panels, (a) CCN<sub>1.0</sub> and (c) CCN<sub>0.1</sub>) or between M01\_S and M01  
878 (right panels, (b) CCN<sub>1.0</sub> and (d) CCN<sub>0.1</sub>). dCCN between M01\_N (M01\_S)  
879 and M01 can be used as a measure of the importance of NPF (SOA).

880 Fig. 6. The period- and domain-averaged size distributions of (a) BC, (b) OA, and (c)  
881 sulfate mass concentrations and (d) number concentrations at a sigma level of  
882 0.895 (~1 km) in six simulations (the simulations are defined in Table 2).

883 Fig. 7. The period- and domain-averaged vertical profiles of (a) CCN<sub>1.0</sub>, (b) CCN<sub>0.1</sub>, (c)  
884 BC mass, and (d) OA mass concentrations in six simulations.

885 Fig. 8. (a) The period- and domain-averaged column AAOD in the M10\_SN simulation.  
886 (b) The latitudinal dependence of mean AAOD values in the M10\_SN (black)  
887 and M10\_N (red) simulations normalized by the column AAOD calculated by  
888 assuming externally-mixed BC particles (External). In the External calculation,  
889 all of the internally-mixed BC particles are separated into BC (externally-mixed)  
890 and non-BC (BC-free) particles. (c) The latitudinal dependence of the  
891 contribution of SOA processes to the absorption enhancement by coating  
892 materials. The contribution is calculated from two column AAOD differences:  
893 the fraction of the AAOD difference between the M10\_SN and M10\_N  
894 simulations (M10\_SN – M10\_N) relative to the AAOD difference between the

895 M10\_SN simulation and the external calculation (M10\_SN – External).  
896 Fig. 9. The period-averaged impacts of (left panels) BC aging and (right panels) SOA  
897 on SSA at 1 km (a & b), the heating rate by aerosols at 1 km (c & d), and the  
898 change in the downward solar flux by aerosols at the surface (e & f). The  
899 contributions of BC aging and SOA are estimated from the difference between  
900 the M10\_SN and M01\_SN simulations and between the M01\_SN and M01  
901 simulations, respectively. In the bottom two panels, the combined effects of  
902 BC aging and SOA (the difference between the M10\_SN and M01 simulations)  
903 are also shown for (g) the heating rate by aerosols and (h) the change in the  
904 downward solar flux by aerosols at the surface. The period-averaged values  
905 are calculated offline using the data at 12:00 local time (03:00 UTC) between 24  
906 March and 26 April.

907 Fig. 10. Summary of the sensitivity of the mass and number concentrations and optical  
908 and radiative parameters of aerosols to NPF, BC aging, and SOA. The red  
909 (blue) lines indicate positive (negative) impacts on individual aerosol parameters  
910 (black boxes). The impact of NPF is calculated from the difference between  
911 the M01\_N and M01 simulations. The impact of SOA is calculated from the  
912 difference between the M10\_SN and M10\_N simulations. The impact of BC  
913 aging is the difference in each parameter between when the BC mixing state is  
914 resolved (the M10\_SN simulation) and when the average mixing state is used  
915 (all BC particles are assumed to be internally mixed) (the M01\_SN simulation).  
916 The change in BC mass concentrations is due to the change in BC hygroscopicity  
917 (mixing state) and resulting wet removal processes. The change in absorption

918 is mainly due to the change in the lens effect. The percentages shown in black  
919 boxes are calculated from the difference between the M10\_SN and M01  
920 simulations.

921

**Table 1.** Summary of chemical schemes and representations adopted in ATRAS-MOSAIC and the original MOSAIC

Item or chemical process	ATRAS-MOSAIC	Original MOSAIC
Aerosol emission	40 nm – 10 $\mu\text{m}$ (pure BC, BC-free)	40 nm – 10 $\mu\text{m}$ (internally-mixed)
Gas-phase chemistry	SAPRC99 with SOA precursors	CBM-Z
Photolysis	Fast-J	Fast-J
Number of total aerosol bins	128 (maximum)	8
Number of aerosol size bins	20	8
Number of mixing state bins	10 (maximum)	1
Condensation and evaporation	MOSAIC (2-D)	MOSAIC
Coagulation	Two-dimensional semi-implicit method	Semi-implicit method
Nucleation	Activation-type/kinetic nucleation (PBL <sup>a</sup> ) and binary homogeneous nucleation (FT <sup>a</sup> ) at 1 nm	Binary homogeneous nucleation at 40 nm
Organic aerosol formation	Volatility basis-set	Primary organic aerosol only
CCN activation	Multiple hygroscopicities for each size bin	Single hygroscopicity for each size bin
Aqueous-phase chemistry	Fahey and Pandis, 2001	Fahey and Pandis, 2001
Optical properties	Multiple mixing states for each size bin	Single mixing state for each size bin
Dry and wet deposition	Easter et al., 2004	Easter et al., 2004

<sup>a</sup> PBL, planetary boundary layer; FT, free troposphere.

**Table 2.** List of model simulations

Simulation	Number of aerosol bins	BC mixing state	NPF	SOA
M10_SN	128	On (10 bins)	On	On
M10_N	128	On (10 bins)	On	Off
M08_SN	104	On (8 bins)	On	On
M06_SN	80	On (6 bins)	On	On
M04_SN	56	On (4 bins)	On	On
M01_SN	20	Off	On	On
M01_N	20	Off	On	Off
M01_S	12	Off	Off	On
M01	12	Off	Off	Off

**Table 3.** Period- and domain-averaged aerosol mass and number concentrations at an altitude of about 1 km (sigma level of 0.895) at noon

Parameter	Unit	M10_SN	M10_N	M08_SN	M06_SN	M04_SN	M01_SN	M01_N	M01_S	M01
PM <sub>2.5</sub>	$\mu\text{g m}^{-3}$	15.1	12.1	15.1	15.2	15.1	15.1	12.1	15.0	12.1
BC	$\mu\text{g m}^{-3}$	0.463	0.469	0.463	0.460	0.449	0.422	0.422	0.421	0.422
OA	$\mu\text{g m}^{-3}$	4.30	1.43	4.31	4.32	4.30	4.31	1.44	4.30	1.45
SO <sub>4</sub>	$\mu\text{g m}^{-3}$	3.84	3.79	3.85	3.84	3.83	3.84	3.80	3.82	3.80
NH <sub>4</sub>	$\mu\text{g m}^{-3}$	1.89	1.87	1.89	1.89	1.88	1.88	1.87	1.87	1.87
NO <sub>3</sub>	$\mu\text{g m}^{-3}$	1.72	1.71	1.71	1.71	1.69	1.68	1.68	1.68	1.68
CCN <sub>1.0</sub>	$\text{cm}^{-3}$	2434	2409	2438	2446	2443	2469	2472	2063	2061
CCN <sub>0.2</sub>	$\text{cm}^{-3}$	1079	968	1081	1083	1079	1088	991	1034	959
CCN <sub>0.1</sub>	$\text{cm}^{-3}$	498	427	498	499	497	495	425	491	430

**Table 4.** Period- and domain-averaged optical and radiative parameters at noon

Parameter	Unit	Layer	M10 SN	M10 N	M08 SN	M06 SN	M04 SN	M01 SN	M01 N	M01 S	M01
AOD	---	Column	0.311	0.246	0.311	0.312	0.311	0.309	0.244	0.312	0.246
AAOD	---	Column	0.0152	0.0138	0.0152	0.0160	0.0163	0.0183	0.0176	0.0183	0.0176
SSA	---	PBL <sup>a</sup>	0.930	0.921	0.930	0.927	0.925	0.910	0.894	0.911	0.895
Heating rate	K day <sup>-1</sup>	PBL <sup>a</sup>	0.424	0.395	0.425	0.443	0.454	0.513	0.492	0.513	0.494
Downward flux	W m <sup>-2</sup>	Surface	-34.9	-28.4	-35.0	-35.7	-35.7	-37.4	-31.5	-37.5	-31.5

<sup>a</sup> PBL, planetary boundary layer.

Figure 1

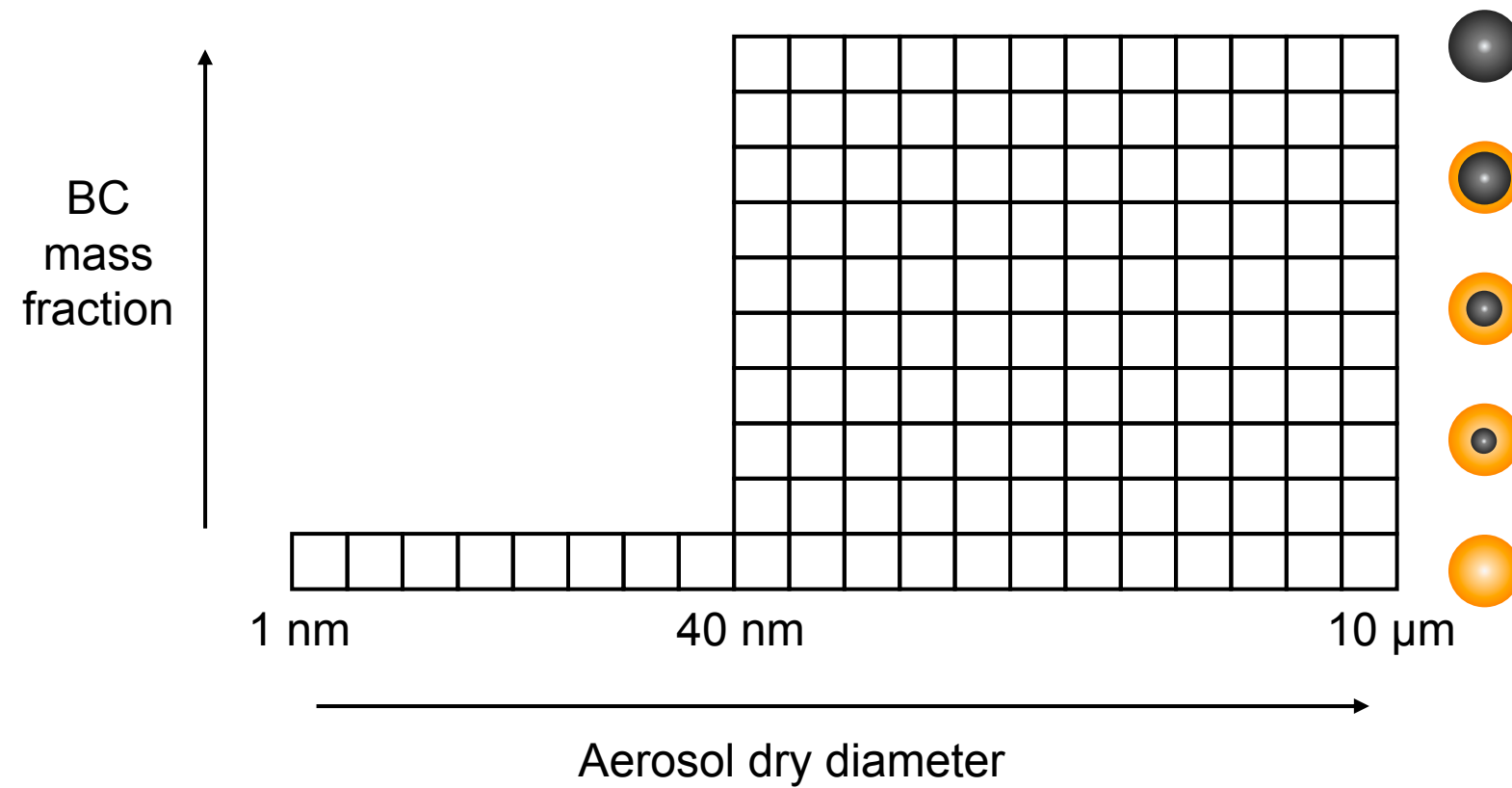


Figure 2

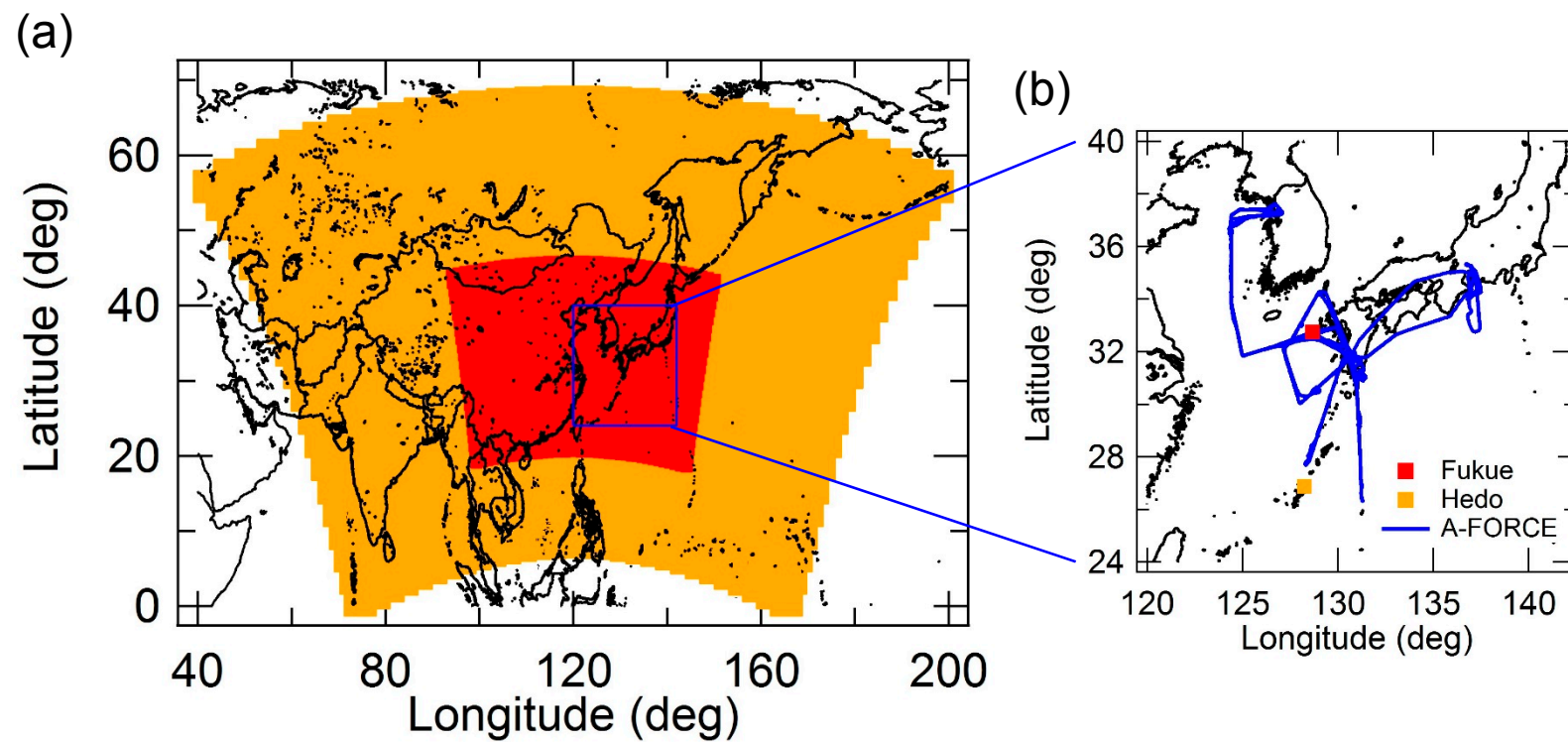


Figure 3

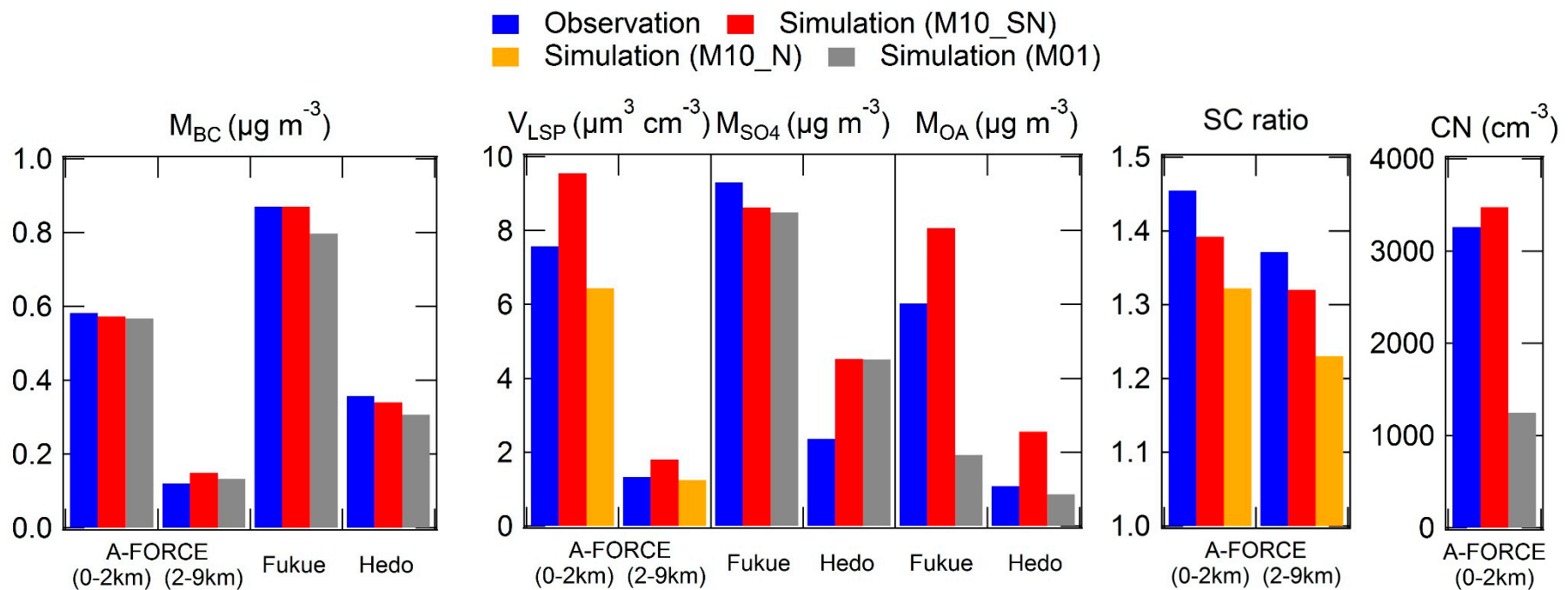


Figure 4

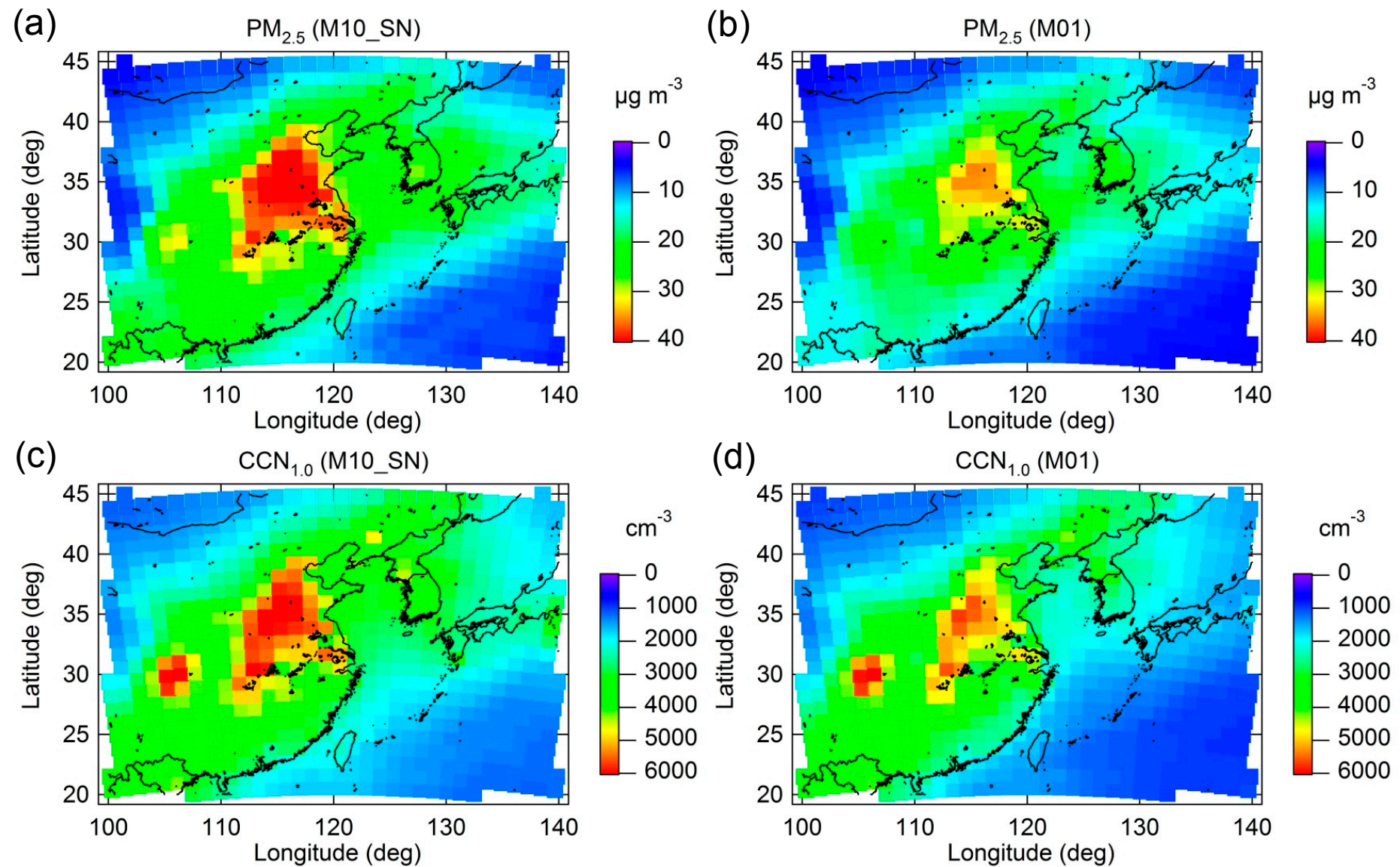


Figure 4 (cont.)

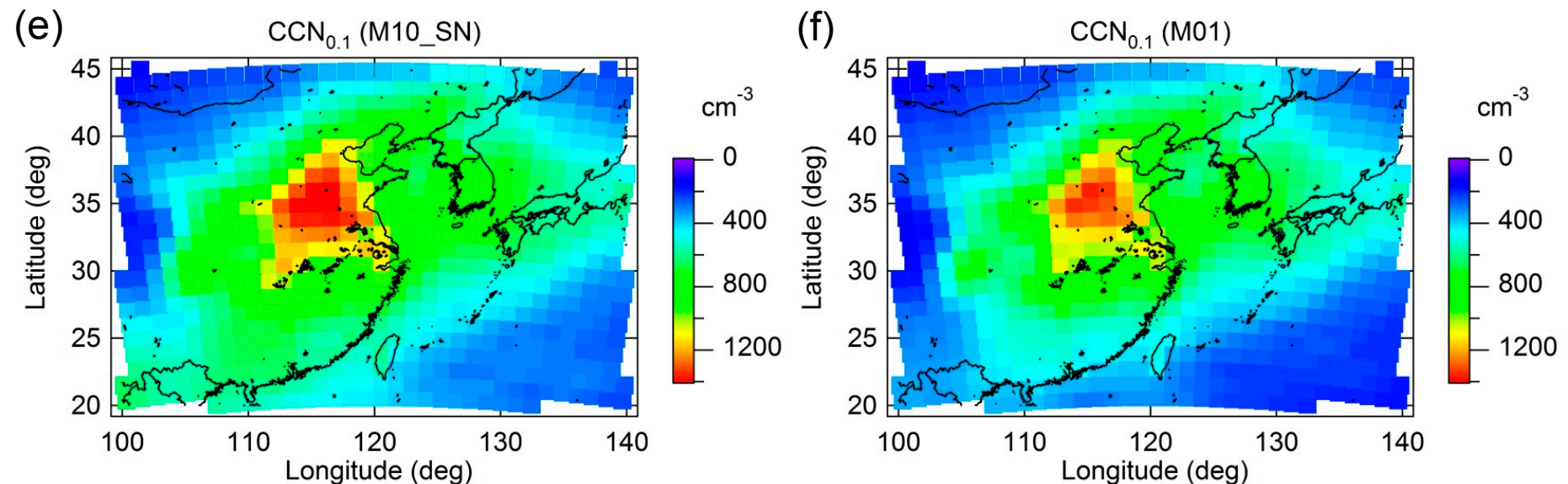


Figure 5

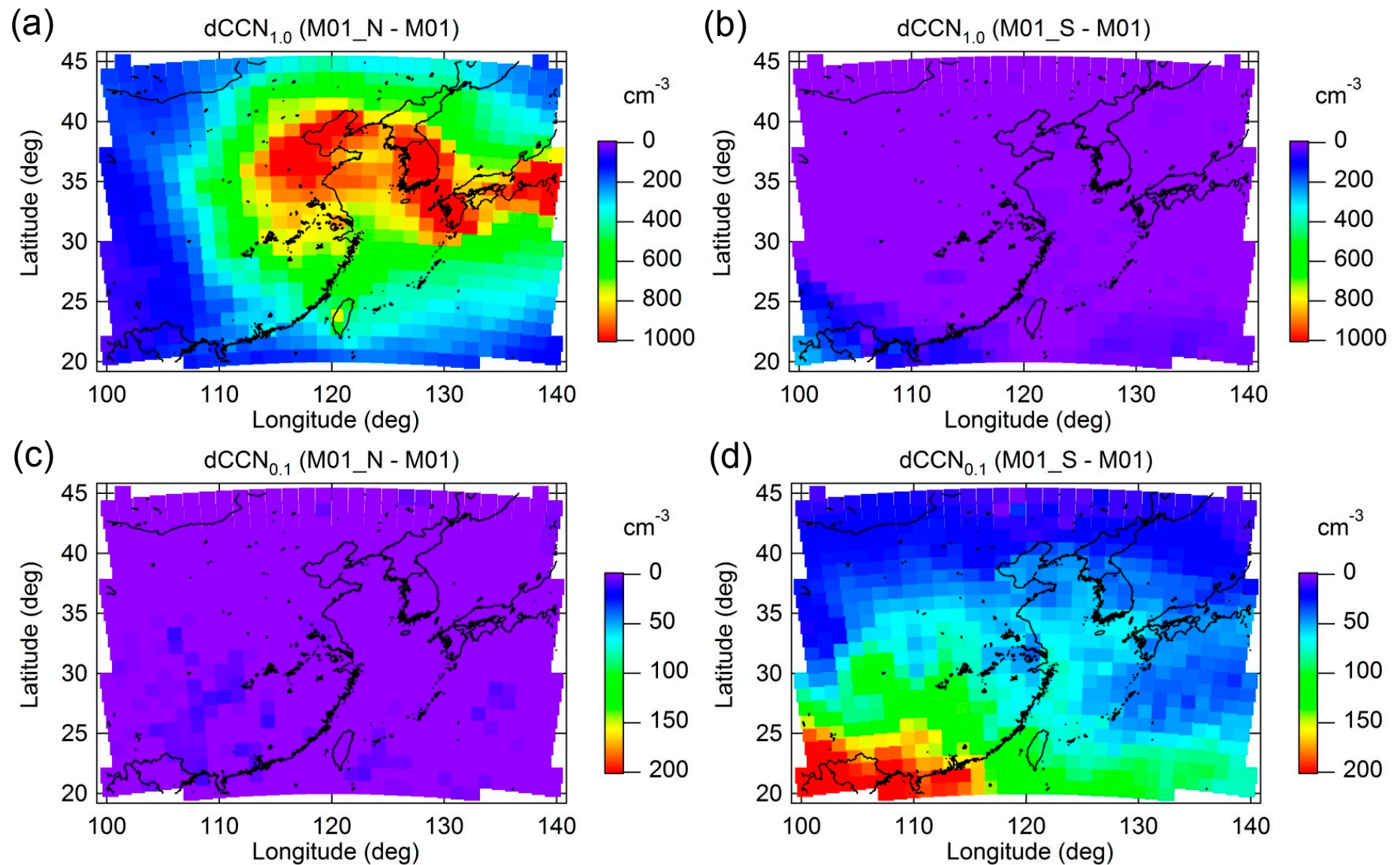


Figure 6

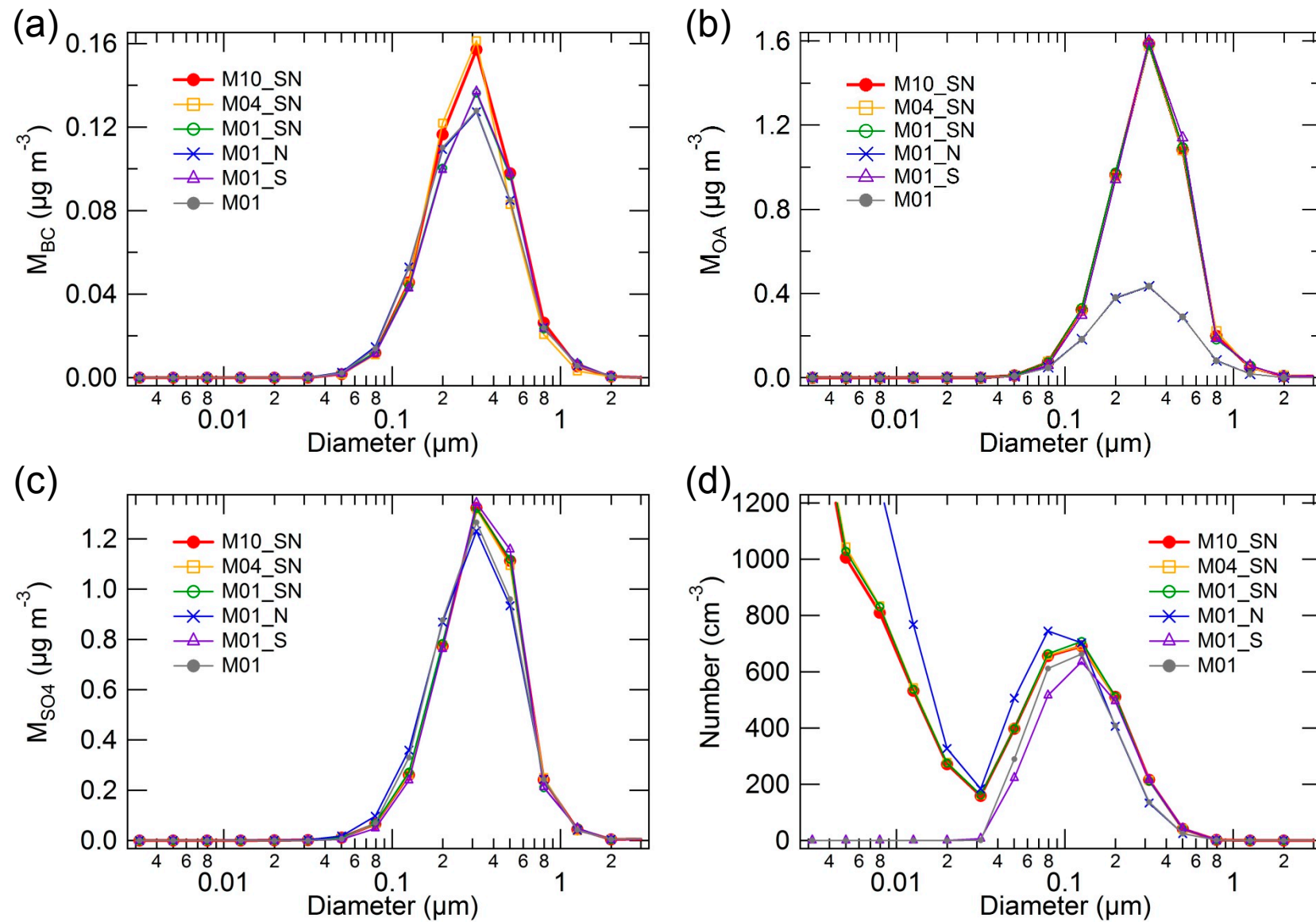


Figure 7

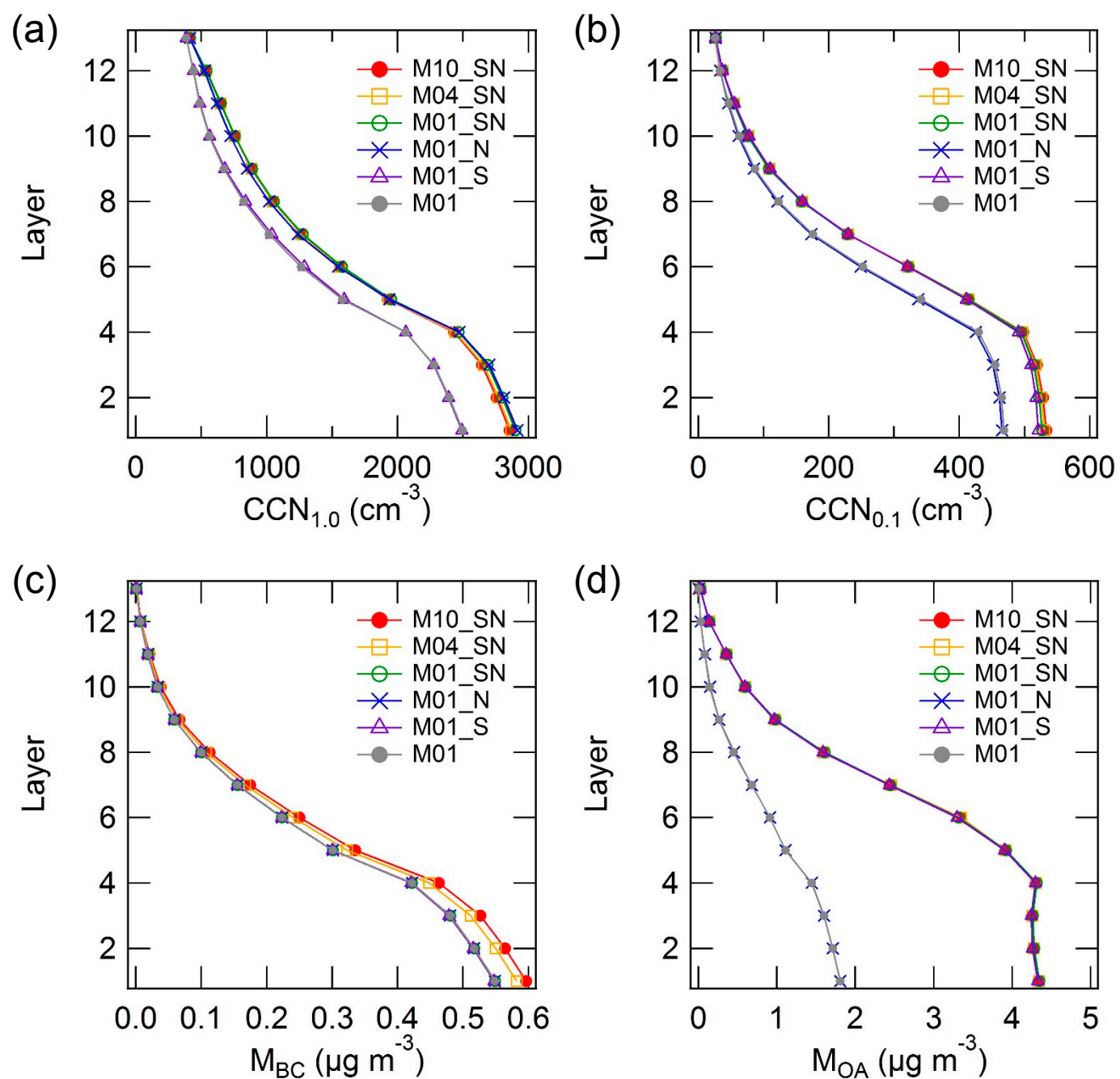


Figure 8

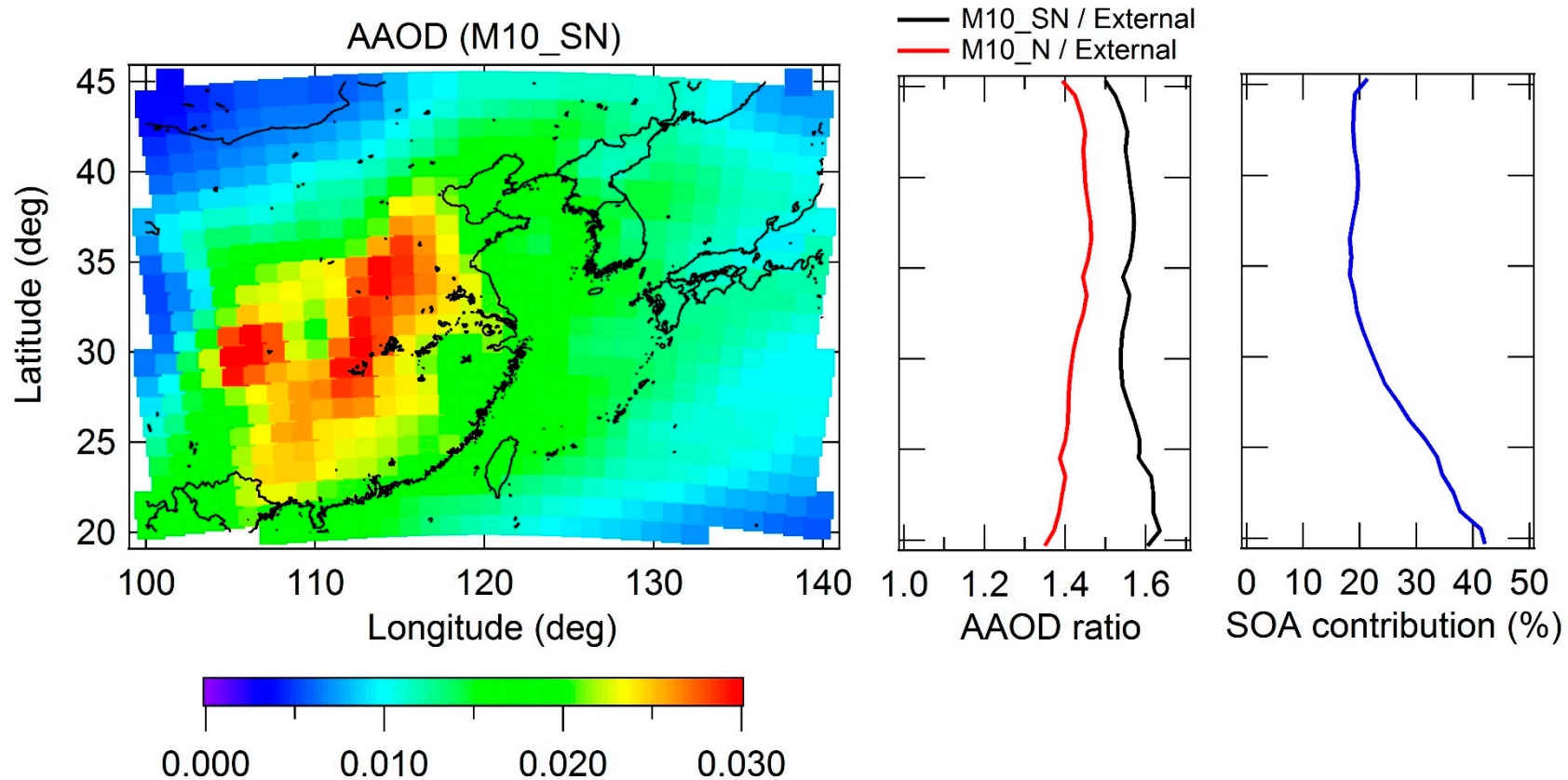


Figure 9

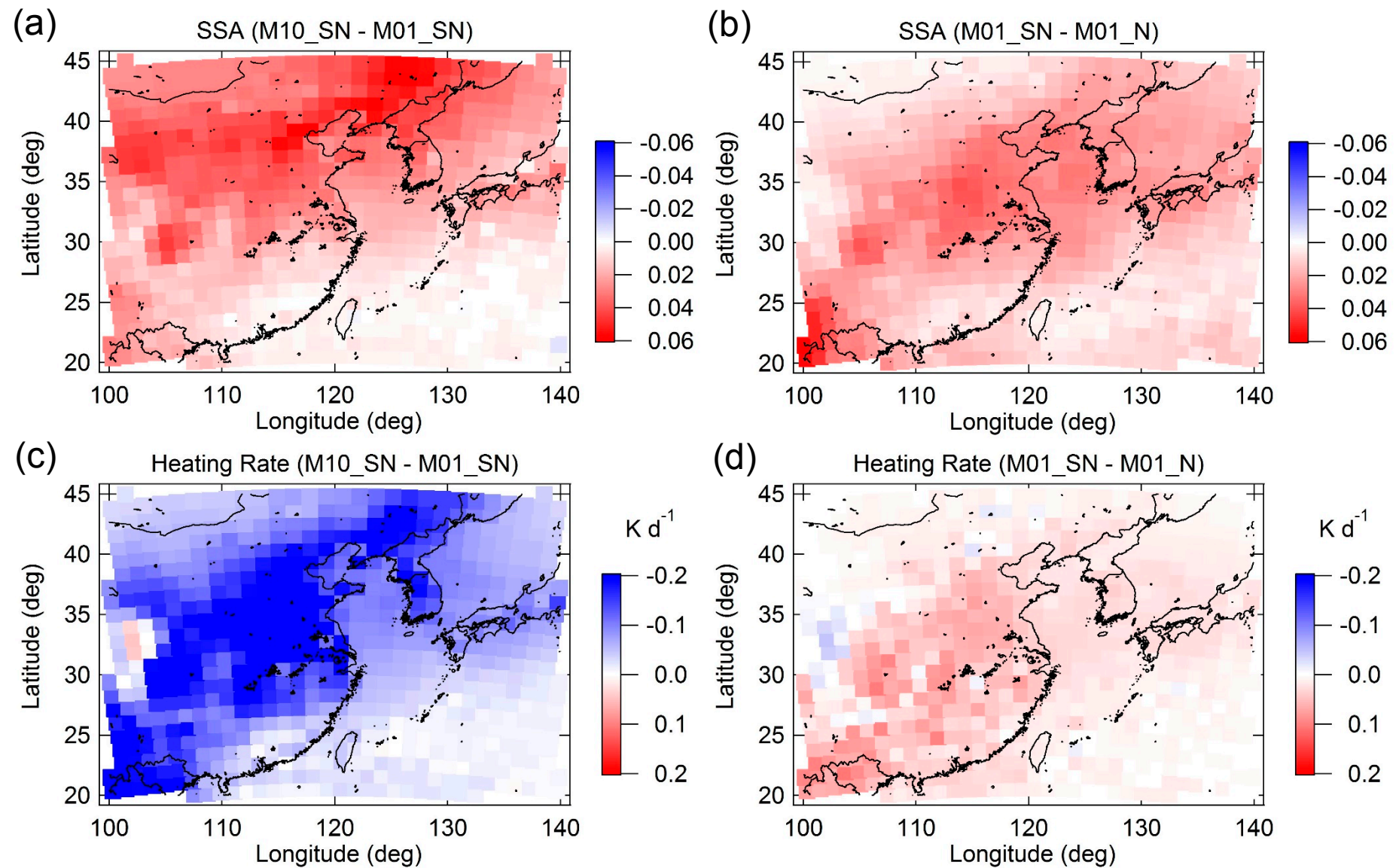


Figure 9 (cont.)

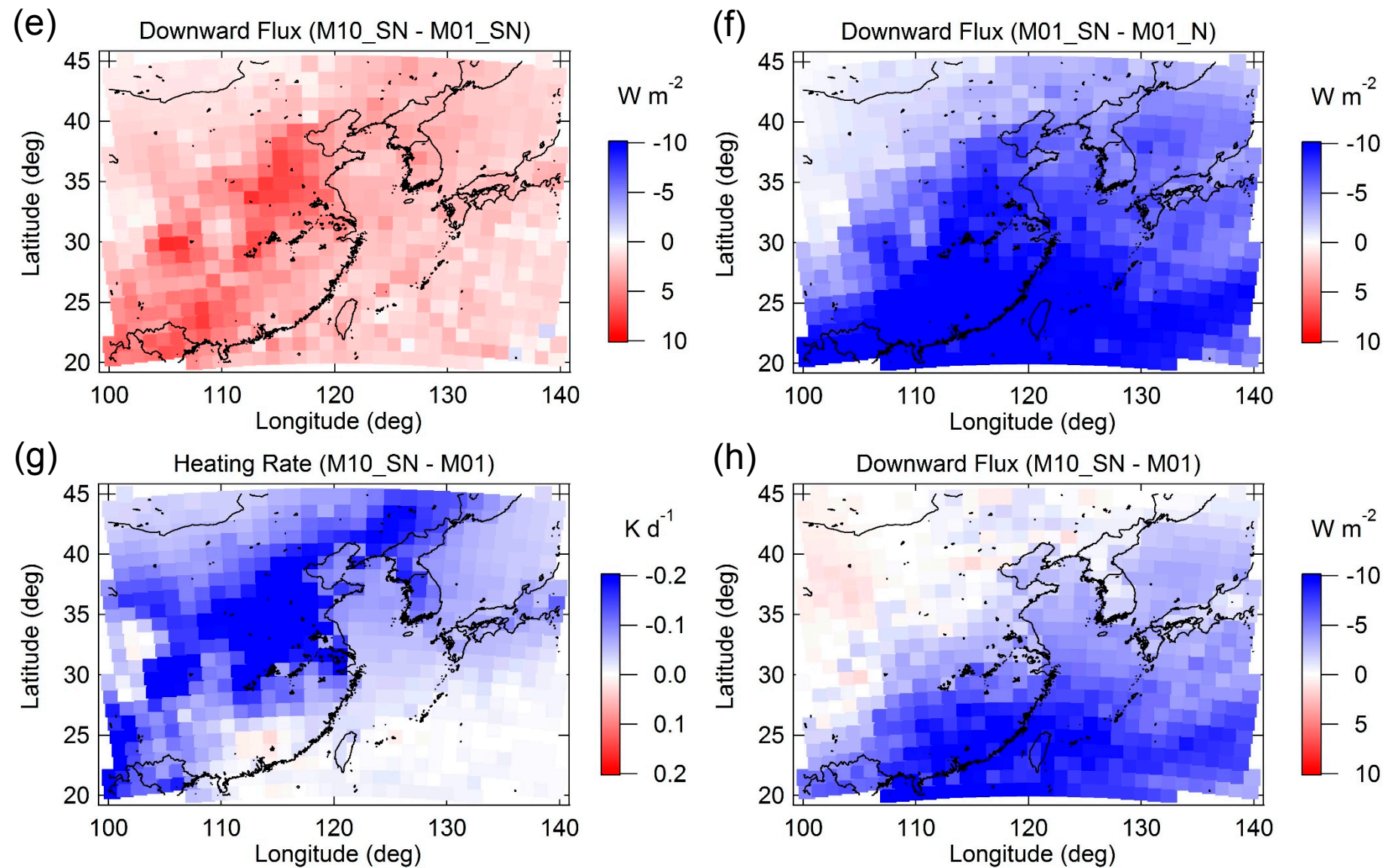


Figure 10

